Biophysical *Journal*
Article

Biophysical Society

An NMR look at an engineered PET depolymerase

Cyril Charlier,[1] Sabine Gavalda,[2] Vinciane Borsenberger,[2] Sophie Duquesne,[1] Alain Marty,[2] Vincent Tournier,[2] and Guy Lippens[1,*]
[1]Toulouse Biotechnology Institute (TBI), Université de Toulouse, CNRS, INRAE, INSA, Toulouse 31077, France and [2]Carbios, Biopôle Clermont Limagne, Saint-Beauzire, France

ABSTRACT Plastic environmental pollution is a major issue that our generation must face to protect our planet. Plastic recycling has the potential not only to reduce the pollution but also to limit the need for fossil-fuel-based production of new plastics. Enzymes capable of breaking down plastic could thereby support such a circular economy. Polyethylene terephthalate (PET) degrading enzymes have recently attracted considerable interest and have been subjected to intensive enzyme engineering to improve their characteristics. A quadruple mutant of Leaf-branch Compost Cutinase (LCC) was identified as a most efficient and promising enzyme. Here, we use NMR to follow the initial LCC enzyme through its different mutations that lead to its improved performance. We experimentally define the two calcium-binding sites and show their importance on the all-or-nothing thermal unfolding process, which occurs at a temperature of 72°C close to the PET glass transition temperature. Using various NMR probes such as backbone amide, methyl group, and histidine side-chain resonances, we probe the interaction of the enzymes with mono-(2-hydroxyethyl)terephthalic acid. The latter experiments are interpreted in terms of accessibility of the active site to the polymer chain.

SIGNIFICANCE Plastic pollution is a persistent challenge worldwide. The PET polymer, used for plastic bottles, bags, and textiles, is not easily degraded. Novel processes aimed at not only destroying the polymer but truly recycling it in a form that gives access again to the same high-quality plastics are needed. Biobased methods relying on enzymes that can depolymerize PET might constitute an alternative to chemical catalysts to fully recover the monomers needed for renewed production of high-quality PET. Here, we follow by solution NMR spectroscopy the LCC enzyme through its four mutations that turn it into a PETase that outperforms all other enzymes so far in a close-to-industrial process, and provide an experimental basis for understanding its improved characteristics.

INTRODUCTION

Plastic pollution is a persistent challenge worldwide and results from our lifestyle with its dependency on plastic bottles, bags, and textiles (1). Under the form of microparticles, mostly generated by domestic and commercial laundering of synthetic textiles (2), human-made plastics are blown by the winds (3,4), fall down on land as plastic rain (5), and end up in the seas where they concentrate in fish and other seafood (6). Of especial importance is the polyethylene terephthalate (PET) polymer, whose annual production exceeds 80 million tons (7). Although a general consumer product because of its low price and outstanding performance in terms of solidity and durability, these latter characteristics also hamper its degradation (8). Novel processes aimed at not only downsizing or destroying the polymer but truly recycling it in a form that gives access again to the same high-quality plastics are sorely needed (9).

Biobased methods relying on enzymes that can depolymerize the PET—so-called PET depolymerases, PET hydrolases, or PETases that all indicate the same enzyme category under EC 3.1.1.101 poly(ethylene terephthalate) hydrolase—have in this regard attracted major attention (10,11). They potentially constitute an alternative to chemical catalysts to fully recover the terephthalic acid (TA) and monoethylene glycol (EG) monomers needed for renewed production of high-quality PET (12). The *Is*PETase from *Ideonella sakaiensis*, a microorganism that can grow on PET as its sole carbon source (13), has been the starting point for an extensive enzyme engineering effort in many laboratories (14–17). The Leaf-branch Compost Cutinase (LCC) was another enzyme identified early on in a metagenomic screen as a PET depolymerase (18). Through

Submitted March 24, 2022, and accepted for publication June 30, 2022.
*Correspondence: glippens@insa-toulouse.fr
Cyril Charlier and Sabine Gavalda contributed equally to this work.
Editor: Scott Showalter.
https://doi.org/10.1016/j.bpj.2022.07.002

rigorous testing and extensive protein engineering, a quadruple mutant was presented (19) that outperforms all other enzymes thus far in a close-to-industrial process (20). The crystal structure of the original LCC enzyme (Protein Data Bank accession (PDB): 4EB0 for the active enzyme (21)), beyond visualizing the catalytic triad (S165/H242/D210) and the Y95/M166 residues forming an oxyanion hole whose backbone amides are involved in transition state stabilization, thereby served as a template to engineer an additional disulfide bridge (D238C/S283C), leading to the LCC-CC enzyme variant with a significant increase in melting temperature (T_m). The F243I mutation (in the D238C-S283C-F243I LCC-ICC enzyme) was added, based on increased specific activity toward enzymatic PET depolymerization. Ultimately, because of increased thermostability, the Y127G mutation was implemented in the aforementioned variant and led to the highly active LCC-ICCG (F243I-D238C-S283C-Y127G) enzyme variant of LCC (PDB: 6THT for the S165A inactive form) (19).

We present here an in-depth NMR study of the LCC enzyme and of the different variants of LCC that led to LCC-ICCG, thereby reinforcing the experimental basis for understanding the improved characteristics of the enzymes. We confirm that the different mutations do not perturb the overall structure, map the calcium-binding sites—notably the one that was replaced by a disulfide bridge in the LCC-CC variant—and demonstrate an increase of T_m for the latter variant in an all-or-nothing process of unfolding. By mapping the chemical shift perturbations (CSP) of amide protons and nitrogens, methyl carbons, and histidine side-chain resonances upon the addition of increasing amounts of mono-(2-hydroxyethyl)terephthalic acid (MHET) to the enzyme, we identify elements of a potential interacting surface between the enzymes and MHET as a surrogate for the polymer chain. For all the NMR probes developed, the MHET-induced CSPs correlate well with the previously determined enzymatic activity of the variants.

MATERIALS AND METHODS

Protein expression and purification

The sample preparation was adapted from Tournier et al. (19). The genes encoding LCC, LCC-CC, LCC-ICC, and LCC-ICCG (all with the inactivating S165A mutation) were expressed in *Escherichia coli* BL21 (DE3) (New England Biolabs, Ipswich, MA). Uniformly labeled ^{15}N and $^{15}N/^{13}C$ proteins were overexpressed in M9 minimum medium (42.3 mM Na_2HPO_4, 22 mM KH_2PO_4, 8.55 mM NaCl, 1 mM $MgSO_4$, 0.1 mM $CaCl_2$, 1× minimum essential medium containing vitamins, 50 μg/mL kanamycin) supplemented with 1 g/L of $^{15}NH_4Cl$ and with 4 g/L D-glucose or 4 g/L [*U*-^{13}C]-D-glucose. Protein expression was induced by adding 0.5 mM isopropyl-1-thio-β-D-galactopyranoside to the cell cultures followed by an overnight incubation at 21°C under agitation. Cells were harvested by centrifugation (5000 × *g*, 20 min, 4°C) and lysed by sonication in the presence of 0.1 mg/mL lysozyme. Lysate was then placed at 70°C for 30 min prior to centrifugation (10,000 × *g*, 30 min, 4°C) and transferred to a desalting column (HiPrep 26/10; GE Healthcare, Chicago, IL) followed by cation exchange column (HiLoad 16/10 SP Sepharose HP; GE Healthcare). A final step of purification was performed using size-exclusion chromatography on a Superdex 200 16/60 instrument (GE Healthcare). Fractions containing the pure proteins were finally concentrated into a buffer containing 25 mM Tris-HCl (pH 7.5) and 100 mM NaCl.

NMR resonance assignment

The experiments for backbone assignment (^{15}N, $^{1}H^{N}$, ^{13}CO, $^{13}C_{\alpha}$) and $^{13}C_{\beta}$ chemical shift resonances were recorded on an 800-MHz spectrometer equipped with a 5-mm cryoprobe with z pulsed-field gradients using a series of two-dimensional (2D) ^{15}N-^{1}H transverse relaxation optimized spectroscopy (TROSY) and three-dimensional (3D) TROSY triple-resonance experiments (HNCO, HN(CA)CO, HNCA, HNCACB, and HN(CO)CACB) (22,23) recorded on samples containing 500 μM $^{15}N/^{13}C$-LCC dissolved in 25 mM Tris-HCl buffer (pH 7.5) with 100 mM NaCl at 30°C. The assignment was confirmed with a 3D Nuclear Overhauser Effect Spectroscopy (NOESY)-TROSY experiment (24) recorded at 900 MHz. All data were processed with NMRPipe (25) and analyzed with NMRFAM-Sparky (26) and/or TopSpin 3.6pl7 (Bruker, Billerica, MA). Spectral dimensions for the HNCO and HN(CA)CO experiments were 2817 Hz (F_1) × 2432 Hz (F_2) × 11,160 Hz (F_3) corresponding to 14 × 30 × 13.94 ppm, with sampling durations of 11.4 ms (t_1), 16.4 ms (t_2), and 184 ms (t_3). RF carriers were set to 4.697 ppm (^{1}H), 118.5 ppm (^{15}N), and 173 ppm (^{13}CO). Respectively 8 (HNCO) and 32 (HN(CA)CO) scans per increment were recorded.

Spectral settings for the HNCA experiment were 8048 Hz (F_1) × 2432 Hz (F_2) × 11,160 Hz (F_2) corresponding to 40 × 30 × 13.94 ppm, with sampling durations of 11.9 ms (t_1), 16.4 ms (t_2), and 184 ms (t_3). RF carriers were set to 4.697 ppm (^{1}H), 118.5 ppm (^{15}N), and 54 ppm ($^{13}C_{\alpha}$), and 8 scans per free induction decay (FID) were recorded. Spectral settings for the HNCACB and HN(CO)CACB, recorded with 16 scans per FID, were identical to those for the HNCA experiment, except for the ^{13}C dimension (F_1) whereby a spectral width of 14,084 Hz corresponding to 70 ppm, with a sampling duration of 9 ms (t_1) with ^{13}C RF carrier set at 40 ppm were used. Spectral dimensions for the 3D $H^{N}H^{N}$-NOESY-TROSY experiment, with a mixing time of 100 ms, were 12,500 (F_1) × 2737 Hz (F_2) × 12,500 Hz (F_3) corresponding to 13.9 × 30 × 13.89 ppm, with sampling durations of 20.5 ms (t_1), 17.5 ms (t_2), and 16.4 ms (t_3). RF carriers were set to 4.697 ppm (^{1}H) and 118.5 ppm (^{15}N). Four scans per increment were recorded.

Assignment of each additional mutant (LCC-CC, LCC-ICC, LCC-ICCG) was verified using 3D TROSY HNCA, HNCO, and eventually HNCACB experiments with similar spectral settings and 30% or 40% nonuniform sampling (27). Spectra were acquired on 500 μM $^{15}N/^{13}C$ samples dissolved in 25 mM Tris-HCl buffer (pH 7.5) with 100 mM NaCl at 30°C. Data were reconstructed using the SMILE software suite (28).

Calcium chemical shift perturbations

The CSP analysis was performed starting from a series of ^{1}H-^{15}N TROSY spectra recorded at 800 MHz and 30°C of uniformly labeled ^{15}N-LCC (200 μM) supplemented with increasing amounts of calcium (Sigma, St. Quentin Fallavier, France), from 0 mM up to 30 mM. The combined ^{1}H,^{15}N CSP values were calculated for each residue from the differences in the amide proton $^{1}H^{N}$ ($\Delta\delta_{H}{}^{N}$) and nitrogen ^{15}N ($\Delta\delta_{N}$) chemical shifts between the free (0 mM Ca^{2+}) and the calcium-saturated (30 mM Ca^{2+}) states using the formula (29)

$$\mathrm{CSP} = \sqrt{(\Delta\delta_{H^N})^2 + 0.1(\Delta\delta_N)^2}.$$

Dissociation constants (K_D) were fitted to the theoretical binding curve using an in-house Python script

$$\Delta\delta_{obs} = \Delta\delta_{max}\frac{\left([P]_t + [L]_t + K_D\right) - \sqrt{\left([P]_t + [L]_t + K_D\right)^2 - 4[P]_t[L]_t}}{2[P]_t},$$

where $[P]_t$ and $[L]_t$ are the protein and the ligand concentration, $\Delta\delta_{obs}$ is the chemical shift change for a given peak relative to its position in the free form of the protein, and $\Delta\delta_{max}$ is the maximal difference in chemical shift between the same peak in the spectra of the free form of the protein and that of the Ca^{2+}-saturated protein.

Thermal stability measurements

We measured ^{1}H-^{15}N TROSY spectra on a 200-μL sample of ^{15}N-labeled LCC (concentration 500 μM, buffer 25 mM Tris-HCl (pH 7.5) with 100 mM NaCl) in a 3-mm tube using a BBI 3-mm probe on the 800-MHz instrument. For the first part of the series, we measured a spectrum every 10°C from 30°C to 60°C, and then every 2°C from 60°C to 74°C. Time between measurements was 15 min for the first part of the series with 10°C temperature increase, and 5 min for the series with 2°C temperature increase, allowing for the temperature rise and shimming of the magnet. The spectral recording itself took 2 min for the one-dimensional (1D) spectrum and 21 min for the 2D spectrum.

Interaction with MHET

MHET was prepared as described earlier (19). Starting from a stock solution of MHET in water that was brought to the same pH as the protein solution, we lyophilized different aliquots containing an amount of MHET equal to 1, 2, 4, or 10 mM of MHET in 200 μL volume. Exact dosing was performed by recording a 1D proton spectrum with a 15-s relaxation delay of two aliquots of MHET (4 mM and 10 mM) in 200 μL of buffer and comparing the integral of the MHET signals with that of the reference trimethyl silyl propionate (TSP). The latter TSP concentration was dosed by comparing its integral with that of a commercial calibrated succinate standard (Sigma-Aldrich, Darmstadt, Germany). The 1D spectrum equally showed the presence of a small amount of terephthalate (TA), which was evaluated at 5%–6% of the MHET. In a control experiment, we recorded the spectra of LCC in the presence of 600 μM TA (6% of 10 mM MHET, the maximal concentration used), and found no CSPs.

NMR titration experiments with MHET were recorded at 800 MHz and 60°C on 100 μM samples of ^{15}N-^{13}C uniformly labeled proteins. All data were referenced to TSP and were acquired using the following parameters.

- *$^{1}H/^{15}N$ mapping*. Series of ^{1}H-^{15}N band-selective excitation short-transient TROSY (30) were recorded with spectral widths of 2919 Hz (F_1) × 12,820 Hz (F_2) corresponding to 36 × 16.02 ppm and sampling durations of 21.9 ms (t_1) and 39.9 ms (t_2). RF carriers were set to 4.697 ppm (^{1}H) and 118.5 ppm (^{15}N), and 32 scans per FID were recorded.

The CSP was calculated for every residue using the formula shown above and using the data in the absence of MHET and in the presence of 4 mM MHET.

- *$^{1}H/^{13}C$ methyl mapping*. Series of ^{1}H-^{13}C heteronuclear single-quantum coherence (HSQC) were recorded with spectral widths of 4024 Hz (F_1) × 11,160 Hz (F_2) corresponding to 20 × 13.94 ppm and sampling durations of 15.9 ms (t_1) and 45.8 ms (t_2). RF carriers were set to 4.697 ppm (^{1}H) and 18 ppm (^{13}C), and 16 scans per FID were recorded.
- *$^{1}H\varepsilon/^{13}C\varepsilon$ histidine mapping*. Series of ^{1}H-^{13}C heteronuclear multiple-quantum coherence (HMQC) were recorded with spectral widths of 8048 Hz (F_1) × 11,160 Hz (F_2) corresponding to 40 × 13.94 ppm and sampling durations of 31.8 ms (t_1) and 45.8 ms (t_2). RF carriers were set to 4.697 ppm (^{1}H) and 120 ppm (^{13}C), and 32 scans per FID were recorded.

The combined ^{1}H,^{13}C CSP was calculated using the following formula:

$$CSP = \sqrt{(\Delta\delta_{H^N})^2 + 0.3(\Delta\delta_C)^2}.$$

RESULTS

Identification of calcium-binding sites by NMR titration

All NMR experiments presented in our study have been carried out using the inactive mutants of the LCC enzyme or its variants, in which the catalytic serine 165 was replaced by an alanine residue. Expression levels of the inactive mutants proved far superior, and crystal structures of LCC-S165A (PDB: 6THS) and LCC (PDB: 4EB0) showed a minimal structural variation (root-mean-square deviation 0.27 Å) due to this point mutation (Fig. S1) (19,21). In addition, the inability to perform interaction studies with the active forms of other PET depolymerases was previously demonstrated (14). For clarity's sake, in this paper we designate by LCC the enzymes containing the S165A inactivating mutation.

We first obtained for LCC at 30°C a near-complete site-specific assignment of the backbone resonances (92% of ^{1}H, ^{15}N chemical shifts) using a set of regular triple-resonance TROSY-based experiments (Fig. S2). The broad dispersion of the amide ^{1}H chemical shifts from 10.7 ppm to 5.4 ppm is characteristic for a correctly folded protein in solution. When applying the Chemical Shift Index (CSI) on the combined C_α/C_β/CO frequencies (31,32), all secondary structure elements present in the X-ray structure could be identified. The ^{1}H-^{15}N amide signals corresponding to residues R65 to G73 composing part of the short α2 helix in the loop connecting β1 and β2 strands were missing in the spectrum (Fig. S1). Their absence could be caused by a rapid amide hydrogen exchange with the solvent and/or a conformational averaging with enhanced dynamics, as suggested by the higher B-factors for this region in the X-ray

crystal structure (19). Crosspeaks for some other isolated residues were also missing from the spectrum. Whereas A165, the inactivating mutation of the catalytic S165, could be assigned to the most downfield shifted amide nitrogen at 135.1 ppm (folded in at 105.1 ppm in the spectrum of Fig. S2), the amide resonance of its direct neighbor, M166, whose main-chain amide group forms the oxyanion hole together with that of Y95 (18,21), could not be identified.

Previous work indicated that metal ions generally increase the thermal stability of PET hydrolases (33,34). The stabilizing effect of calcium (Ca^{2+}) on LCC was evaluated by circular dichroism (CD) as an 8.4°C T_m increase at 10 mM of Ca^{2+} (21), whereas differential scanning fluorimetry (DSF) yielded a value of 9.3°C with saturating amounts of Ca^{2+}(19). We set up an NMR titration assay to probe experimentally, at a per-residue scale, the interaction of Ca^{2+} with LCC. The position of some ^{1}H-^{15}N crosspeaks progressively changed upon increasing Ca^{2+} concentrations from 2.5 to 30 mM, without any significant line broadening (Fig. 1 *A*). CSPs calculated for each Ca^{2+} concentration were used to determine calcium-binding curves for the residues whose resonance proved most sensitive to the addition of calcium (29) (Fig. 1 *B* and Table S1). Two distinct binding sites with high CSP values were identified (Fig. 1, *C* and *D*). The preferential metal ion-binding site is located near the aspartate 238 and confirms the previous identification of the triplet E208/D238/S283 as calcium-binding site 2 by topological search through other cutinase homologs (19). For this site, a K_D value of the order of 3 mM was determined (Fig. 1 *B*), in good agreement with the CD-derived value (21). In addition, we observed substantial CSPs for residues T192, D193, F196, T198, N225, and L226 (Fig. 1 *C*). These define a second binding site of weaker affinity between the loop connecting β6 and β7 and the helices facing this loop in the 3D structure (Fig. 1 *D*), in agreement with the D204-T206 Ca^{2+}-binding site number 3 observed in Cut190 (Fig. S3) (35,36). Altogether, these data show that the NMR assignment of the ^{1}H-^{15}N TROSY experiment can be used to map the physical interaction, at a per-residue scale, of individual amino acids with potential interactors of the enzyme.

Improved thermostability with a disulfide bridge

The thermal stability of the LCC enzyme was enhanced through replacement by a disulfide bridge of the predicted and here experimentally verified calcium-binding site 2 (19). This T_m improvement proved of particular importance, as the enzyme needs to remain catalytically active for a long time at elevated temperatures (60°C–72°C), close to the glass transition temperature of PET (37), in order to fully degrade the PET material (38). To monitor whether unfolding starts in certain parts of the enzyme, the thermal stability of LCC was explored by measuring ^{1}H-^{15}N spectra as a function of temperature (Figs. 2 and S4). By recording spectra every 10°C between 30°C and 60°C and every 2°C from 60°C up to 72°C, we could follow many individual peaks and hence obtain their assignment at high temperature. However, at 74°C, the spectrum of LCC completely disappeared, indicating a global aggregation event (Fig. 2, *A* and *B*). The 1D proton spectrum acquired before the 2D ^{1}H-^{15}N experiment clearly illustrates the complete disappearance of signals in both the amide (Fig. 2 *A*) and methyl region (Fig. 2 *A*, *inset*) and eliminates possible artifacts of spectral disappearance due to the temperature dependency of water exchange. Unfolding and aggregation were irreversible, as no workable spectrum could be obtained after cooling the sample from 74°C to lower temperatures. We next repeated the experiment in the presence of a saturating amount of Ca^{2+} (30 mM) (Fig. 2, *C* and *D*). Even though we could not go beyond 74°C with our experimental NMR setup, the fact that the spectrum of Ca^{2+}-loaded LCC remains intact at 74°C confirms that full occupancy of the Ca^{2+}-binding sites stabilizes the LCC enzyme.

Triple-resonance NMR experiments on a ^{15}N,^{13}C-labeled sample of the LCC D238C-S283C (LCC-CC) mutant indicated that the 3D structure is minimally affected by these two mutations, as ^{15}N and $^{13}C_\alpha$ chemical shifts are very similar to those of LCC, with the only differences located in the direct vicinity of the two mutations (Fig. S5, *A*, *C*, and *D*). The C_β and C_α carbon chemical shifts of respectively 37.9 ppm and 52.5 ppm for Cys238 (Fig. S5 *B*), and a C_β value of 36.0 ppm for Cys283, confirm that the disulfide bridge indeed is formed in this mutant (Fig. S5 *E*) (39). We then increased the temperature of this sample stepwise up to 74°C and found that in the absence of Ca^{2+}, the spectrum of LCC-CC remained intact (Fig. 2, *E* and *F*). Whereas the temperature stability of the LCC enzyme under our NMR conditions is limited to 72°C with a global unfolding/aggregation at 74°C, saturating the calcium-binding site or replacing it by a disulfide bond hence increases the overall thermal stability of the enzyme.

Mapping MHET interaction with LCC using backbone amides

Mapping of the physical interaction between the PET chains and the enzyme is hampered by the poor solubility in aqueous solution of the polymeric substrate. Even a simple TA_2EG_3 molecule with two TA and three EG moieties could not be detected in our NMR conditions. We thus used the MHET molecule consisting of a single TA esterified with a single EG as a minimal soluble proxy for PET. We recorded a series of ^{1}H-^{15}N TROSY spectra on the LCC-CC enzyme with increasing concentrations of MHET (Figs. 3 *A* and S6 *A*). Based on the thermostability of the enzyme described above and on our demonstrated ability to record high-quality spectra at elevated temperatures (Fig. 2, *E* and *F*), we performed our titration experiments at 60°C to

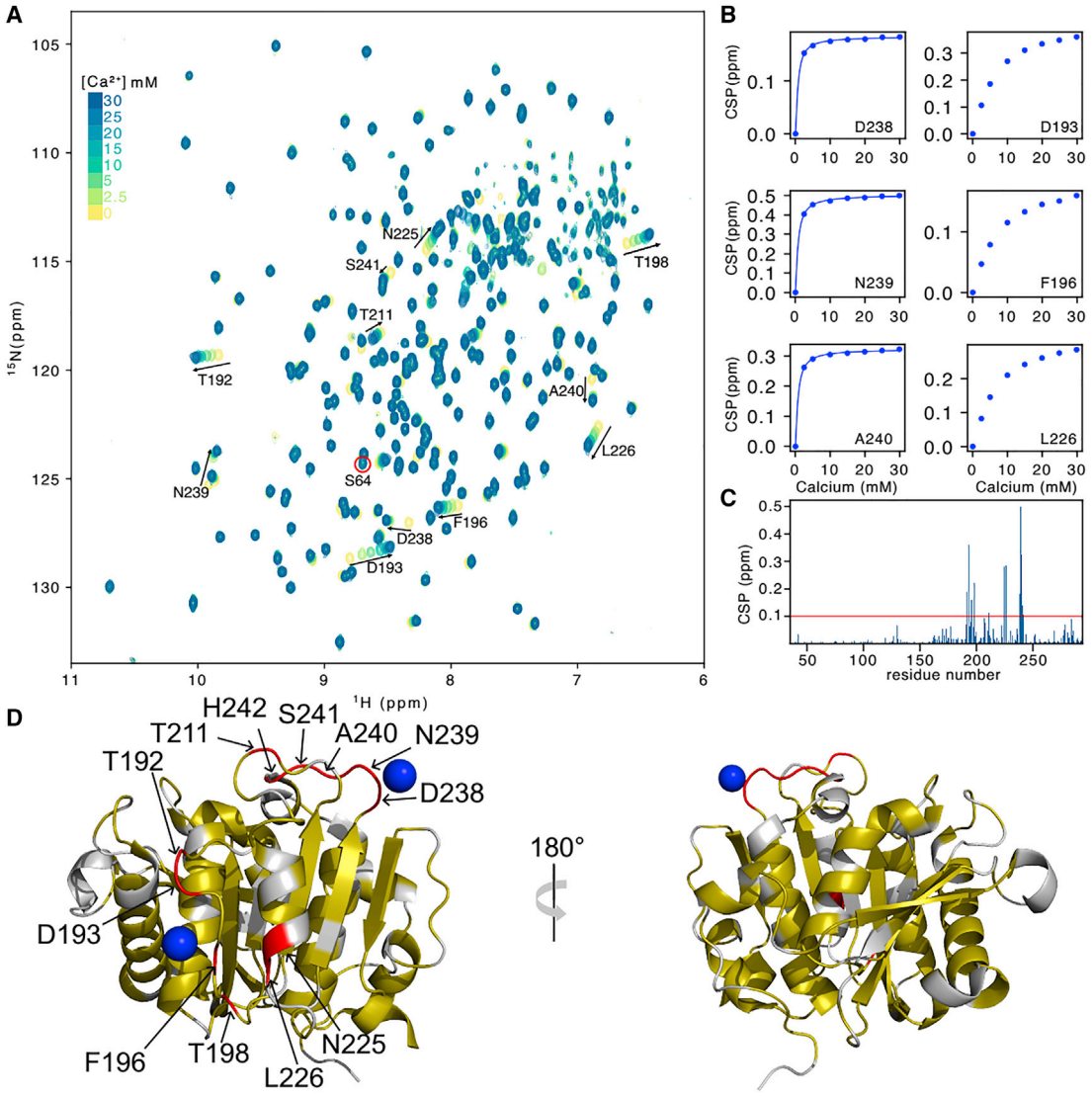

FIGURE 1 NMR detects two Ca^{2+}-binding sites on LCC. (*A*) Titration of ^{15}N-labeled LCC with increasing concentrations of Ca^{2+} from 2.5 to 30 mM as followed by two-dimensional ^{1}H-^{15}N TROSY spectra. Residues with a significant CSP are labeled. The peak of S64 is circled in red and shows no CSP at all. (*B*) Titration curves obtained from ^{1}H-^{15}N spectra determine a K_D value of $\approx$3 mM for the Ca^{2+}-binding site centered on D238 and $> \approx$10 mM for the site centered on D193. (*C*) CSPs between the free LCC and the LCC in the presence of 30 mM Ca^{2+}, plotted along the primary sequence. (*D*) CSPs shown on the 3D structure of LCC (PDB: 6THS). Residues for which no data are available are shown in gray, residues with $0 <$ CSP <0.1 ppm are shown in yellow, and residues with CSP > 0.1 ppm are shown in red (*red line* in *C*). The two Ca^{2+} ions represented by the blue spheres are taken from the Cut190 structure (PDB: 5ZNO). To see this figure in color, go online.

better match the temperature conditions applied in an industrial reactor for enzymatic PET depolymerization.

In agreement with MHET being a product of the enzyme rather than its preferred substrate, we found that a large excess was needed before observing the first CSPs on the LCC-CC spectrum. The most pronounced effect was observed for amide crosspeaks of the V212-A213 dipeptide, immediately downstream of the catalytic D210 residue (Figs. 3 *A* and S6 *A*). The peak of the other residue of the catalytic triad, S165, replaced by A165 in the inactive mutant, also shifts appreciably upon addition of MHET (Figs. 3 *A* and S6 *A*). Finally, amide resonances of the direct neighbors of H242, the catalytic histidine, F243, and A244 are equally impacted by the added MHET (Figs. 3 *C* and S6 *A*).

As the F243I mutation was previously shown to increase the specific activity of the enzyme (19), we produced and assigned the spectrum of ^{15}N,^{13}C-labeled LCC-ICC protein. Not unexpectedly, replacing the Phe aromatic ring by an Ile aliphatic side chain leads to observable shifts for the amide crosspeaks of the T211-V212-A213 loop, in agreement with those three residues being all at less than 10 Å from the center of the aromatic ring (Fig. S7).

An identical titration experiment of the LCC-ICC enzyme with increasing amounts of MHET shows CSPs in the same

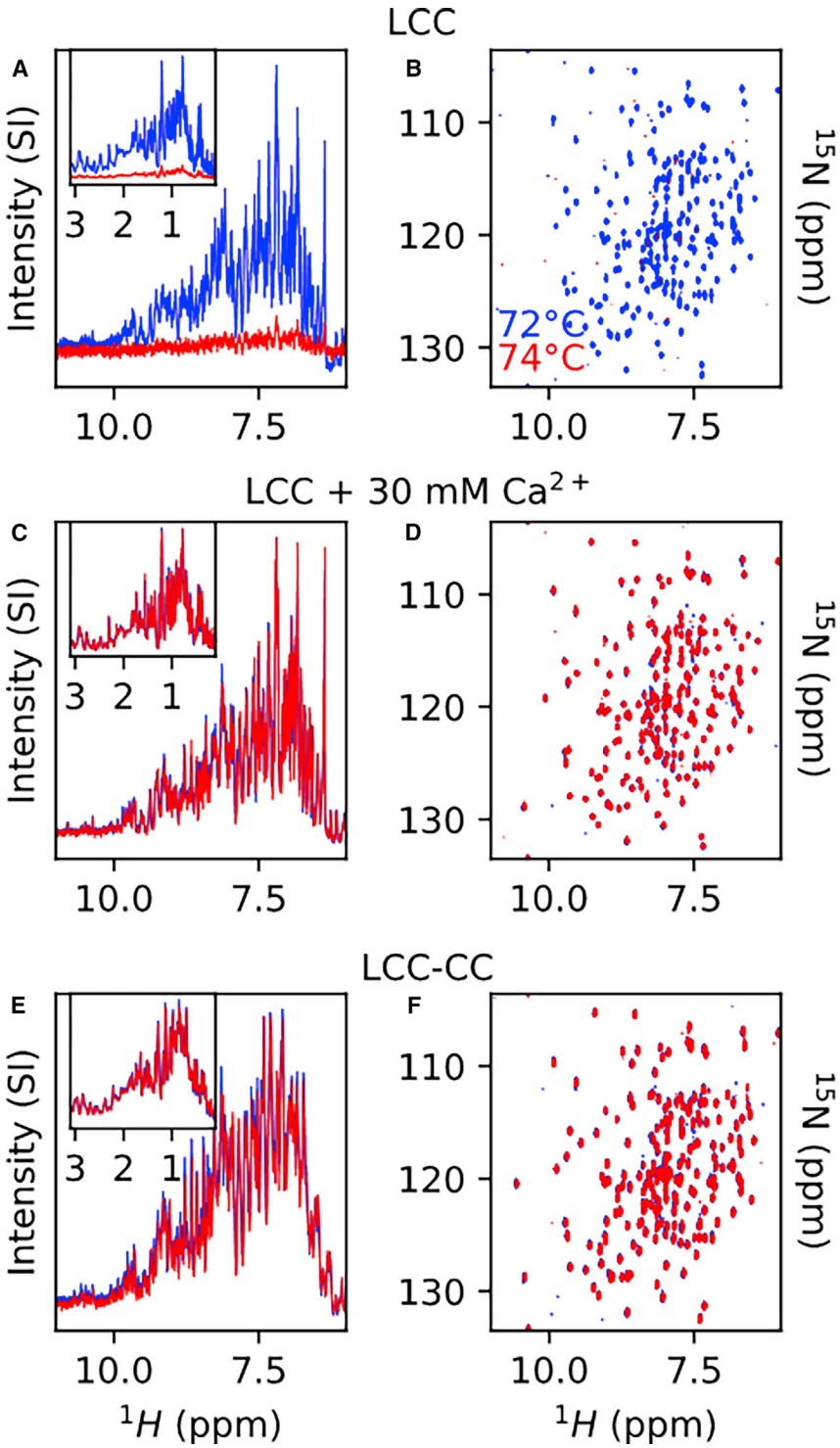

FIGURE 2 Ca^{2+} or the engineered disulfide bridge stabilize the enzyme beyond 74°C. (*A* and *B*) LCC without Ca^{2+} at 72°C (*blue*) and 74°C (*red*). (*C* and *D*) LCC saturated with 30 mM Ca^{2+} at 72°C (*blue*) and 74°C (*red*). (*E* and *F*) LCC-CC at 72°C (*blue*) and 74°C (*red*). (*A*, *C*, and *E*) The main panels represent the amide region of the proton spectra, and the insets display the methyl region. (*B*, *D*, and *F*) ^{1}H-^{15}N TROSY spectra. To see this figure in color, go online.

direction as before for the V212-A213 amide crosspeaks (Figs. 3 *B* and S6 *B*), but their amplitude increases by 50% when compared with the results from LCC-CC (Fig. S6 *C*). This is not only the case for residues in the active site but also for residues in a larger sphere around the catalytic triad (Fig. 3 *C* and Table S2). Effectively, resonances for G94, for G206, and for T188 are perturbed in the LCC-ICC spectrum upon addition of MHET (Fig. S8). Within the 3D structure of the LCC-ICC, G94 is a nearest neighbor of Y95 that together with M166 forms the oxyanion hole stabilizing the transition state (18,21). Residue G206 is localized on the β-strand preceding the catalytic

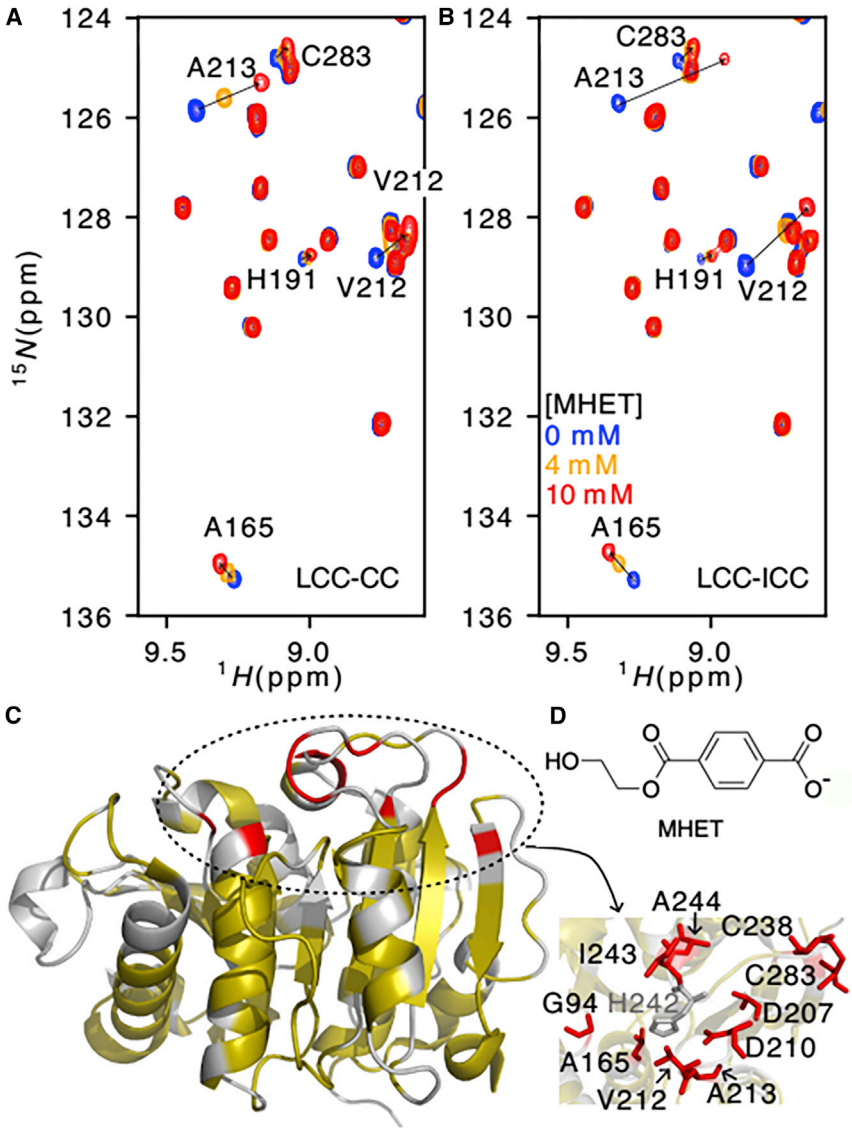

FIGURE 3 MHET interaction specificity at the enzyme surface. ^{1}H-^{15}N TROSY spectra of 100 μM LCC-CC (*A*) or 100 μM LCC-ICC (*B*) in the absence of MHET (*blue*) and in the presence of 4 mM (*orange*) and 10 mM (*red*) MHET, at 60°C. (*C*) CSPs calculated from the spectra of LCC-ICC with 0 and 10 mM of MHET shown on the LCC-ICCG structure (PDB: 6THT). Residues for which no data are available are shown in gray, residues with 0 < CSP <0.07 ppm are shown in yellow, and residues with 0.07 ppm < CSP are shown in red. The panel on the right indicates the residues identified with the higher CSPs surrounding the catalytic histidine H242. (*D*) Molecular structure of the MHET ligand. To see this figure in color, go online.

D210, and the residue T188 is just beneath the H242 imidazole ring.

Methyl mapping further refines the interaction site

Beyond physical interactions, amide proton and nitrogen chemical shifts are extremely sensitive to numerous other structural parameters such as electrostatics, H-bonding, or ring current shifts, leading to a less straightforward interpretation in terms of physical interaction. Aliphatic groups are less subject to electrostatic contributions, and ring current shifts are mostly short-ranged. Moreover, as ^{13}C chemical shifts are conformation dependent, they represent reporters of structural rearrangement and hence of direct binding-induced effects (29,40). Therefore, we also mapped the influence of increasing MHET concentrations on the methyl region of the ^{1}H-^{13}C HSQC spectrum of ^{15}N/^{13}C-labeled LCC-CC and LCC-ICC proteins. Excellent resolution was obtained by recording 64 complex points in the indirect dimension, and allowed singling out of the three methionine methyl groups (matching the three Met present in LCC) by their lack of a ^{13}C–^{13}C coupling constant (Fig. S9 *A*). One methionine methyl resonates at a most unusual ^{1}H chemical shift of 0 ppm both in the LCC-CC and LCC-ICC enzymes (Fig. S9 *A*, *blue inset*). It was assigned to M166, whose methyl is sandwiched between both aromatic rings of W190 and Y127 (Fig. S10) and thereby experiences an important ring current shift (41,42). This same methyl group of M166 in both LCC-CC and LCC-ICC variants shifts appreciably when MHET is added (Fig. 4, *A* and *E*; Fig. S11). The extent of the methyl CSPs thereby follows the trend observed for the amide CSPs, with CSPs in LCC-CC consistently smaller than their equivalent CSPs in LCC-ICC.

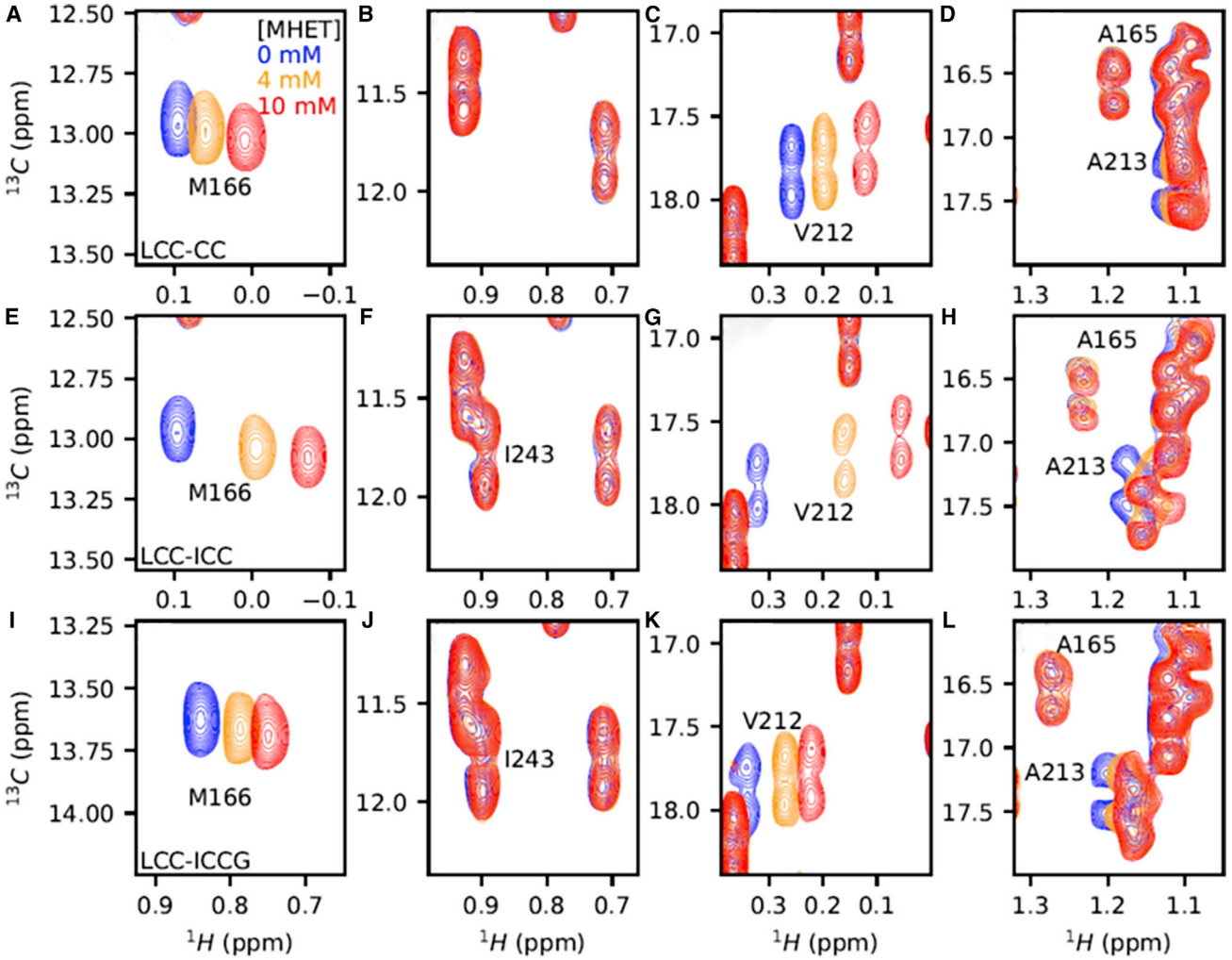

FIGURE 4 Methyl signals upon interaction with MHET at 60°C. Selected regions from ^{1}H-^{13}C HSQC spectra of LCC-CC (*A–D*), LCC-ICC (*E–H*), and LCC-ICCG (*I–L*) in the absence of MHET (*blue*) and in the presence of 4 mM (*orange*) and 10 mM (*red*) MHET. To see this figure in color, go online.

Further exploiting the availability of the ^{1}H-^{13}C spectra of the different mutants, we also readily assigned the δ methyl of I243, absent from the spectrum of LCC-CC (with its F243) but present in LCC-ICC (Fig. 4, *B*, *F*, and *J*). Surprisingly, this methyl does not shift upon titration with MHET (Fig. 4, *F* and *J*), questioning whether a direct interaction between MHET and the side chain at position 243 exists.

Because general methods to assign all methyls of a protein are still in progress (43–50), we focused mostly on the assignment of those methyl resonances that were perturbed by MHET binding. A second methyl group significantly shifting upon MHET addition was assigned to V212 (Fig. 4, *C*, *G*, and *K*). Assignment was based on 1) its close proximity to the aromatic ring of F243 in LCC-CC and subsequent shift between the spectra of LCC-CC and LCC-ICC (Fig. 4, *C* and *G*), 2) the identification of their proton chemical shift from the NOESY-^{1}H, ^{15}N TROSY strips for the T211-V212-A213 peptide (Fig. S12), and 3) the symmetrical NOE contact toward the amide proton of V212 in the strip of the ^{1}H-^{13}C NOESY spectrum (Fig. S12). Interestingly, the other methyl group of V212, although in a more crowded region of the spectrum, is equally perturbed upon addition of MHET (Fig. S11).

Alanine methyl groups can be assigned in a more systematic manner, combining their ^{1}H frequency from the NOESY-^{1}H, ^{15}N TROSY experiment with the $^{13}C_{\beta}$ frequency from the HNCACB spectrum (Fig. S13). We thereby identified A213's methyl that is visibly perturbed by MHET, whereas its neighbor in the spectrum, the A165 methyl in the active site, shows up as a broader peak that only slightly shifts upon addition of MHET (Fig. 4, *D*, *H*, and *L*).

We finally produced and assigned the LCC-ICCG (F243I-D238C-S283C-Y127G) variant that was previously published as the optimal compromise between thermal stability and intrinsic activity (19). Definite confirmation of the previous M166 methyl assignment came from its 0.8 ppm downfield shift in the LCC-ICCG versus LCC-ICC spectrum (Fig. S9 *B*), where the Y127G mutation removes the

contribution to the shielding of the M166 methyl by the Y127 aromatic ring (Fig. S10). The comparison of the methyl CSPs from the LCC-ICCG spectrum upon addition of MHET with those of LCC-CC and LCC-ICC emphasized intermediate CSP values for its M166 and V212 methyl signals (Figs. 4 *I* and S14 *A*). Similar intermediate CSP values upon addition of MHET were also observed when comparing the ^{1}H, ^{15}N backbone CSPs from the LCC-ICCG variant with those of LCC-CC and LCC-ICC (Figs. S14 *B* and S15).

Histidine imidazole side chain signals upon interaction with MHET

Attempting to peer directly into the active site, we turned to the histidine imidazole side-chain resonances. With six histidines, the full assignment required an important number of experiments, which will be presented elsewhere. Importantly, though, we were able to assign all six imidazole Hε/Cε signals in the three variants (Fig. 5, *A–C*), with the catalytic H242 Cε resonating consistently most upfield, whereas it is the Hε proton of H218 with its close stacking to the aromatic ring of W190 (Fig. S16) that is shifted most upfield.

We then repeated the titration experiments of all three mutants with MHET and recorded ^{1}H-^{13}C HMQC spectra at 60°C along the titration (Fig. 5, *A–C*). Perturbations are most pronounced for the His242 imidazole ring, in agreement with this histidine belonging to the catalytic triad. The CSP for His164, whose Hε imidazole proton is at 3.7 Å from that of the His242 ring, is fivefold lower than that of His242, and it is not clear whether the effect is direct or mediated by a possible His242 ring reorientation. The same is true for the Hε/Cε correlation of His218, whose imidazole ring stacks directly to the side chain of W190. The equivalent W185 in the *Is*PETase was identified as a substrate-binding residue with a wobbling conformation (14,51). Although we did not assign the tryptophan side-chain resonances, the small CSP for the His218 Hε/Cε resonance could well reflect the binding of MHET to the W190 side chain and its concomitant reorientation. Importantly, however, the spectra of the histidine Hε/Cε correlations confirmed the previously described tendencies of the amide and methyl CSPs. Effectively, all imidazole Hε/Cε CSPs are more pronounced for LCC-ICC than for both other variants, LCC-CC and LCC-ICCG (Fig. 5 *D*).

DISCUSSION

PET recycling through enzymatic depolymerization has gained a considerable boost with the identification of *I. sakaiensis*, a microorganism that can degrade and use PET as its main carbon source (13). Its PET-degrading enzyme, the *Is*PET depolymerase, has optimal activity at 40°C, with a major drop in efficiency when used at temperatures above 60°C (13,52). Further optimization of both mesophilic or thermophilic PET depolymerases has heavily relied on numerous high-resolution crystal structures of the *Is*PET depolymerase (14,15,53,54) and related enzymes (21,35,55). Here, we present the first solution NMR analysis of a PETase, the LCC enzyme, assign backbone amide ^{1}H/^{15}N, methyl ^{1}H/^{13}C, and histidine ^{1}Hε/^{13}Cε resonances, and use them as a large number of probes to follow the mutations that have turned LCC into LCC-ICCG (F243I-D238C-S283C-Y127G), an optimized enzyme suitable for PET recycling at an industrial scale (19). The resonance assignments equally form the starting point for a future study of the dynamics of these enzymes, which might be directly related to their function (56,57).

Divalent cations such as Ca^{2+} and Mg^{2+} were previously reported to stabilize different PET depolymerases (33,58–60). For instance, three Ca^{2+}-binding sites were detected in Cut190 crystal structure (PDB: 5ZNO) (60). Sequence alignment with LCC shows that amino acid residues involved in sites 2 and 3 and contributing to the thermal stability of Cut190 (33,60) are conserved in LCC (Fig. S3). When mapping on LCC's crystal structure the CSPs induced by the addition of Ca^{2+}, we experimentally confirmed the D238-S283-E208 site 2 as its highest-affinity Ca^{2+}-binding site (Fig. 1). NMR also detects the third binding site (as defined on Cut190) composed of D193-T195, and shows it has weaker affinity. This site is probably involved in the 3°C additional increase in T_m observed under saturating conditions of Ca^{2+} for the LCC-CC enzyme variant (19), and is occupied by a Ca^{2+} ion in the recent MHET/LCC-ICCG complex structure (PDB: 7VVE; Fig. S17) (61). Finally, the first calcium-binding site, defined by S76, A78, and F81 in Cut190 (33,35), is less well conserved in LCC (Fig. S3). Backbone assignments for these residues in LCC are missing (Fig. S1), but we did not detect any CSP upon addition of Ca^{2+}(Fig. 1) for S64 (equivalent to S75 next to S76 in Cut190), suggesting that the number of Ca^{2+}-binding sites in LCC is limited to two.

As thermostability is a most important characteristic for an effective PETase (17), our high-temperature NMR analysis was aimed at identifying regions of the protein where unfolding would start while other secondary and/or tertiary structures would remain intact upon heating, as was demonstrated for a thermophilic cyclophilin enzyme (62,63). A surprising finding was that despite the elevated pH value of 7.5, amide proton exchange remained limited for all variants, leading to good-quality ^{1}H-^{15}N TROSY spectra up to a temperature of 72°C. Going even higher in temperature (but staying within the safety limit of our cryogenically cooled NMR probe), we observed an all-to-nothing transition for LCC without Ca^{2+}, with a good-quality spectrum at 72°C but a complete signal loss at 74°C, which corresponds to the onset of unfolding as determined by DSF (19) (Fig. 2). Saturating LCC with Ca^{2+} preserved the spectral integrity at 74°C, as did replacing D238/S283 in the

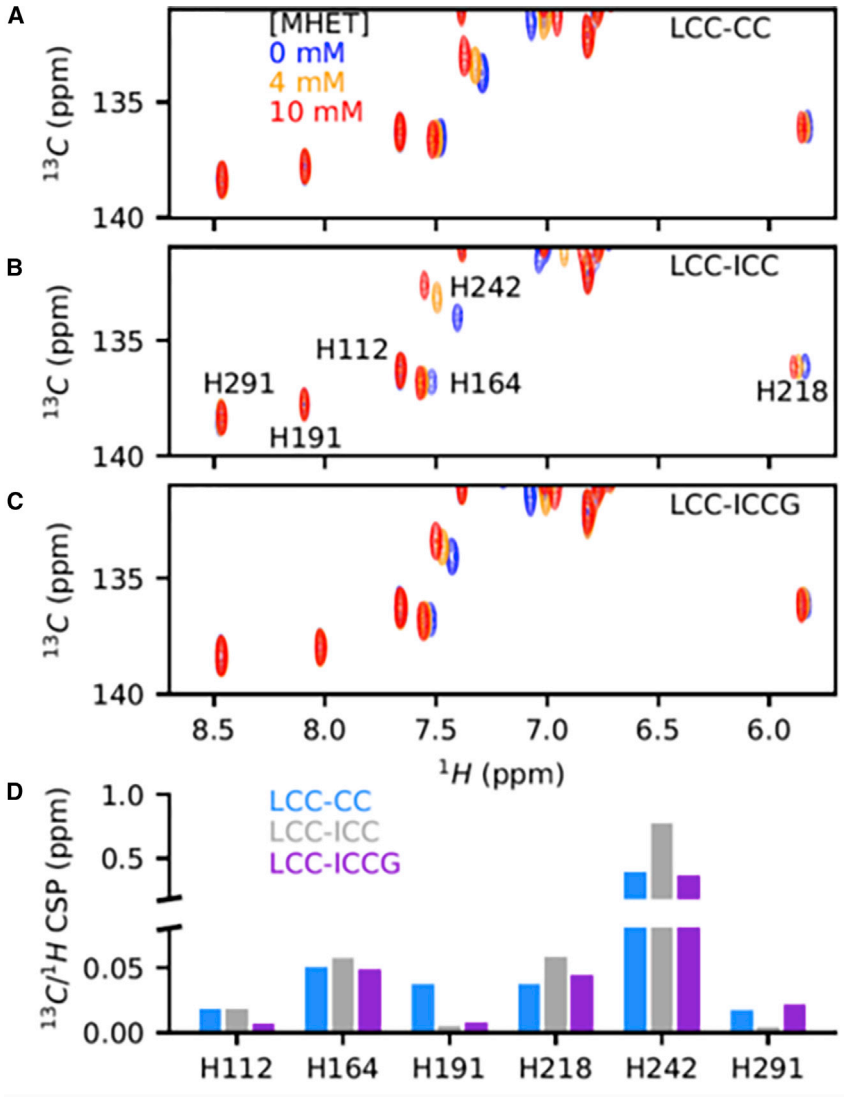

FIGURE 5 Histidine imidazole side-chain signals upon interaction with MHET. Selected region from the ^{1}H-^{13}C HMQC spectrum of LCC-CC (*A*), LCC-ICC (*B*), and LCC-ICCG (*C*) at 60°C in the absence of MHET (*blue*) and in the presence of 4 mM (*orange*) and 10 mM (*red*) MHET. (*D*) ^{1}Hε-^{13}Cε combined CSPs induced by 10 mM MHET for the histidines of LCC-CC (*blue*), LCC-ICC (*gray*), and LCC-ICCG (*violet*). To see this figure in color, go online.

above-determined Ca^{2+}-binding motif with a disulfide bridge, leading to the improved LCC-CC enzyme.

All past efforts to improve the natural PET depolymerases are based on high-resolution crystal structures and subsequent modeling of a short PET chain (14,15,19,53,64,65). However, experimental data on the exact trajectory of the substrate are sorely lacking. Our NMR assignments provide new probes to monitor this interaction, and we present the first results using MHET as a soluble surrogate for the polymer chain. Beyond the three residues of the catalytic triad, our MHET titration experiments identify the major CSPs for the methyls of M166 and V212 (Fig. 4). In excellent agreement with the crystal structure of the *Is*PET depolymerase/HEMT complex (PDB: 5XH3) (14), where the equivalent M161/I208 residues form a clamp holding the aromatic HEMT ring, and with the most recent MHET/LCC-ICCG complex structure (PDB: 7VVE; Fig. S17) (61), these combined experimental results demonstrate that M166 not only contributes to the oxyanion hole via its backbone amide function but also interacts with the PET chain via its side chain, in agreement with its strict conservation in the LCC sequence (18). As large upfield proton CSPs moreover correlate with favorable CH-π interactions (42), we can conclude that the methyls of both M166 and V212 through a CH-π interaction with the aromatic ring of TA contribute to the fine-tuning of the PETase-substrate interaction.

Crystallographic detection of a bound ligand requires a stable and sizable occupancy of the binding site in the crystal. NMR CSPs, however, can detect multiple weak binding sites whereby the ligand only fleetingly perturbs the electronic environment. We observe a non-negligible CSP for A97 upon addition of MHET (Fig. S6). G62, the equivalent residue in Tfcut2 (Fig. S3), was assigned as the culprit for product inhibition of the latter enzyme by MHET (66,67). The G62A mutation in Tfcut2 was found to increase its PET depolymerase activity, an effect that was assigned on the basis of energy calculations to the loss of an inhibitory interaction with a dimer of MHET (67). However, the

CSPs we detect for the amide groups of A97 and its close neighbor A99 (Fig. S6) in the highly efficient LCC variants that we study here indicate that MHET does interact with LCC in this region. The positive effect of the G62A mutation on TfCut2's activity hence might result from an improved interaction with the substrate rather than from preventing an inhibitory interaction with MHET.

The D238C/S283C engineered disulfide bridge in LCC-CC at the position of the here experimentally verified Ca^{2+}-binding site (Fig. 1) anchors the loop preceding the catalytic H242 to the C-terminal β-strand. Although this disulfide bridge effectively raises the limiting temperature beyond which the LCC unfolds and aggregates (Fig. 2), the catalytic activity of the mutant enzyme was found to decrease by nearly 30% (19), even though this disulfide bridge is at a distance of 20 Å from the catalytic site. Whereas this underscores the delicate balance between activity and thermal stability, the large MHET-induced CSPs for the backbone amide resonances of the C238-C283 pair, as well as sizable CSPs for other selected residues from the β7-β8 strands of the central β-sheet and from the α6 helix (Fig. 3 and Table S2) point to a wider interaction of MHET than with the sole active site. It is tempting to speculate that these additional residues might contribute to the interaction of the enzyme with the polymer, but this calls for further experimental evidence. Evidently the disulfide bridge can also influence the dynamics of the active site, whose flexibility is an important factor for activity (51,65,68). Our present NMR assignments open the possibility to experimentally assess these individual contributions to the resulting activity.

We observe a CSP for the amide resonance of I243 (Fig. S6) but cannot exclude that it might result from a reorientation of the neighboring H242 aromatic ring whose Hε/Cε resonance is strongly influenced by the MHET molecule (Fig. 5). A further probe for I243 is its isolated C_δ methyl, whose assignment is unambiguous when we compare the spectra of LCC-CC and LCC-ICC (Figs. 4 and S9). Upon addition of MHET, we observed no CSP at all for this C_δ methyl signal (Fig. 4), excluding its role in fixing a TA moiety through a CH-π interaction as do the methyls of M166 and V212. However, in the absence of a (favorable) direct interaction between the substrate and the residue at position 243, what makes the LCC-ICCG enzyme such an efficient candidate for PET degradation at an industrial scale? Our combined titration data, be it at the level of the backbone amide, methyl, or histidine imidazole ring proton signals, show a gradual shift of the resonances upon increasing ligand concentration, indicative of a rapid exchange for the MHET ligands between the bound and the free state. As shifting resonances in the different variants lie consistently on the same line, we can safely assume that the geometry of the interaction is conserved between the different mutants, with only the fraction of time that MHET spends in the bound state differing between them. The major difference when comparing the CSPs of the mutant enzymes, independently of the probe used, is their increased value upon the F243I mutation in the transition of LCC-CC to LCC-ICC. These data hence experimentally confirm that opening the active site, previously identified as a determining factor for the enzymatic efficiency toward PET degradation (69–71) and here accomplished by removal of the F243 aromatic ring, indeed increases the occupancy of the enzyme active site. Together with the highly optimized thermal stability, this leads to a very active PET depolymerase (19).

We evidently acknowledge that MHET is not the favorable substrate of the PET depolymerases, no more so than molecules such as HEMT, BHET, or even longer model substrates as used in modeling studies. Effectively, the real substrate of PET depolymerases is the PET surface, with its variable degree of order that depends on a number of factors such as temperature and molding (72). Overall, our present NMR study has identified a large number of markers on the enzyme for further investigation of its molecular interaction with such a true plastic surface, be it by solution or solid-state NMR.

SUPPORTING MATERIAL

Supporting material can be found online at https://doi.org/10.1016/j.bpj.2022.07.002.

AUTHOR CONTRIBUTIONS

C.C. and G.L. performed NMR experiments and did data analysis, S.G. produced labeled samples, did biophysical measurements and solved the crystal structure. V.B. provided ligands. G.L., S.D., A.M., and A.T. designed research. C.C. and G.L. wrote the manuscript, and all authors approved the final text.

ACKNOWLEDGMENTS

We thank the ICEO facility of the Toulouse Biotechnology Institute, which is part of the Integrated Screening Platform of Toulouse (PICT, IBiSA), for providing access to protein-purification equipment. We thank Dr. E Cahoreau and L. Peyriga for expert support for the NMR facility of MetaToul (Toulouse Metabolomics & Fluxomics facilities, www.metatoul.fr). Metatoul is part of the French National Infrastructure for Metabolomics and Fluxomics MetabohUB-AR-11-INBS-0010 (www.metabohub.fr), and is supported by the Région Midi-Pyrénées, the ERDF, the Sicoval, and the French Minister of Education & Research, who are all gratefully acknowledged. We thank Dr. F.X. Cantrelle for expert help with the 900 MHz NMR instrument in Lille. Financial support from the IR-RMN-THC Fr3050 CNRS for conducting the research is gratefully acknowledged. This study was supported by Carbios and a grant-in-aid for scientific research (Circular Economy PET project financed by ADEME – contract number 1882C0098).

DECLARATION OF INTERESTS

S.G., V.B., A.M., and V.T. are employees of Carbios. S.D., A.M., and V.T. have filed patents WO 2018/011,284, WO 2018/011,281, and WO 2020/021,118 entitled "Novel esterases and uses thereof."

REFERENCES

1. Iroegbu, A. O. C., S. S. Ray, …, J. P. Sardinha. 2021. Plastic pollution: a perspective on matters arising: challenges and opportunities. *ACS Omega.* 6:19343–19355.
2. Gaylarde, C., J. A. Baptista-Neto, and E. M. da Fonseca. 2021. Plastic microfibre pollution: how important is clothes' laundering? *Heliyon.* 7:e07105.
3. Evangeliou, N., H. Grythe, …, A. Stohl. 2020. Atmospheric transport is a major pathway of microplastics to remote regions. *Nat. Commun.* 11:3381.
4. Brahney, J., N. Mahowald, …, K. A. Prather. 2021. Constraining the atmospheric limb of the plastic cycle. *Proc. Natl. Acad. Sci. USA.* 118. e2020719118.
5. Brahney, J., M. Hallerud, …, S. Sukumaran. 2020. Plastic rain in protected areas of the United States. *Science.* 368:1257–1260.
6. Ribeiro, F., E. D. Okoffo, …, K. V. Thomas. 2020. Quantitative analysis of selected plastics in high-commercial-value Australian seafood by pyrolysis gas chromatography mass spectrometry. *Environ. Sci. Technol.* 54:9408–9417.
7. Singh, A., N. A. Rorrer, …, G. T. Beckham. 2021. Techno-economic, life-cycle, and socioeconomic impact analysis of enzymatic recycling of poly(ethylene terephthalate). *Joule.* 5:2479–2503.
8. Stanica-Ezeanu, D., and D. Matei. 2021. Natural depolymerization of waste poly(ethylene terephthalate) by neutral hydrolysis in marine water. *Sci. Rep.* 11:4431.
9. Taghavi, N., I. A. Udugama, …, S. Baroutian. 2021. Challenges in biodegradation of non-degradable thermoplastic waste: from environmental impact to operational readiness. *Biotechnol. Adv.* 49:107731.
10. Kawai, F. 2021. Emerging strategies in polyethylene terephthalate hydrolase research for biorecycling. *ChemSusChem.* 14:4115–4122.
11. Zhu, B., D. Wang, and N. Wei. 2022. Enzyme discovery and engineering for sustainable plastic recycling. *Trends Biotechnol.* 40:22–37.
12. Thiyagarajan, S., E. Maaskant-Reilink, …, J. van Haveren. 2021. Back-to-monomer recycling of polycondensation polymers: opportunities for chemicals and enzymes. *RSC Adv.* 12:947–970.
13. Yoshida, S., K. Hiraga, …, K. Oda. 2016. A bacterium that degrades and assimilates poly(ethylene terephthalate). *Science.* 351:1196–1199.
14. Han, X., W. Liu, …, R.-T. Guo. 2017. Structural insight into catalytic mechanism of PET hydrolase. *Nat. Commun.* 8:2106.
15. Austin, H. P., M. D. Allen, …, G. T. Beckham. 2018. Characterization and engineering of a plastic-degrading aromatic polyesterase. *Proc. Natl. Acad. Sci. USA.* 115:E4350–E4357.
16. Liu, B., L. He, …, R. Bao. 2018. Protein crystallography and site-direct mutagenesis analysis of the poly(ethylene terephthalate) hydrolase PETase from Ideonella sakaiensis. *Chembiochem.* 19:1471–1475.
17. Brott, S., L. Pfaff, …, U. T. Bornscheuer. 2021. Engineering and evaluation of thermostable IsPETase variants for PET degradation. *Eng. Life Sci.* 22:192–203.
18. Sulaiman, S., S. Yamato, …, S. Kanaya. 2012. Isolation of a novel cutinase homolog with polyethylene terephthalate-degrading activity from leaf-branch Compost by using a metagenomic approach. *Appl. Environ. Microbiol.* 78:1556–1562.
19. Tournier, V., C. M. Topham, …, A. Marty. 2020. An engineered PET depolymerase to break down and recycle plastic bottles. *Nature.* 580:216–219.
20. Sales, J. C. S., A. G. Santos, …, M. A. Z. Coelho. 2021. A critical view on the technology readiness level (TRL) of microbial plastics biodegradation. *World J. Microbiol. Biotechnol.* 37:116.
21. Sulaiman, S., D.-J. You, …, S. Kanaya. 2014. Crystal structure and thermodynamic and kinetic stability of metagenome-derived LC-cutinase. *Biochemistry.* 53:1858–1869.
22. Yamazaki, T., W. Lee, …, L. E. Kay. 1994. A suite of triple resonance NMR experiments for the backbone assignment of 15N, 13C, 2H labeled proteins with high sensitivity. *J. Am. Chem. Soc.* 116:11655–11666.
23. Salzmann, M., G. Wider, …, K. Wüthrich. 1999. TROSY-Type triple-resonance experiments for sequential NMR assignments of large proteins. *J. Am. Chem. Soc.* 121:844–848.
24. Ikura, M., A. Bax, …, A. M. Gronenborn. 1990. Detection of nuclear Overhauser effects between degenerate amide proton resonances by heteronuclear three-dimensional NMR spectroscopy. *J. Am. Chem. Soc.* 112:9020–9022.
25. Delaglio, F., S. Grzesiek, …, A. Bax. 1995. NMRPipe: a multidimensional spectral processing system based on UNIX pipes. *J. Biomol. NMR.* 6:277–293.
26. Lee, W., M. Tonelli, and J. L. Markley. 2015. NMRFAM-SPARKY: enhanced software for biomolecular NMR spectroscopy. *Bioinformatics.* 31:1325–1327.
27. Delaglio, F., G. S. Walker, …, J. P. Marino. 2017. Non-uniform sampling for all: more NMR spectral quality, less measurement time. *Am. Pharm. Rev.* 20:339681.
28. Ying, J., F. Delaglio, …, A. Bax. 2017. Sparse multidimensional iterative lineshape-enhanced (SMILE) reconstruction of both non-uniformly sampled and conventional NMR data. *J. Biomol. NMR.* 68:101–118.
29. Williamson, M. P. 2013. Using chemical shift perturbation to characterise ligand binding. *Prog. Nucl. Magn. Reson. Spectrosc.* 73:1–16.
30. Solyom, Z., M. Schwarten, …, B. Brutscher. 2013. BEST-TROSY experiments for time-efficient sequential resonance assignment of large disordered proteins. *J. Biomol. NMR.* 55:311–321.
31. Wishart, D. S., and B. D. Sykes. 1994. The 13C chemical-shift index: a simple method for the identification of protein secondary structure using 13C chemical-shift data. *J. Biomol. NMR.* 4:171–180.
32. Hafsa, N. E., D. Arndt, and D. S. Wishart. 2015. CSI 3.0: a web server for identifying secondary and super-secondary structure in proteins using NMR chemical shifts. *Nucleic Acids Res.* 43:W370–W377.
33. Then, J., R. Wei, …, W. Zimmermann. 2015. Ca2+ and Mg2+ binding site engineering increases the degradation of polyethylene terephthalate films by polyester hydrolases from Thermobifida fusca. *Biotechnol. J.* 10:592–598.
34. Kawabata, T., M. Oda, and F. Kawai. 2017. Mutational analysis of cutinase-like enzyme, Cut190, based on the 3D docking structure with model compounds of polyethylene terephthalate. *J. Biosci. Bioeng.* 124:28–35.
35. Miyakawa, T., H. Mizushima, …, M. Tanokura. 2015. Structural basis for the Ca(2+)-enhanced thermostability and activity of PET-degrading cutinase-like enzyme from Saccharomonospora viridis AHK190. *Appl. Microbiol. Biotechnol.* 99:4297–4307.
36. Numoto, N., N. Kamiya, …, M. Oda. 2018. Structural dynamics of the PET-degrading cutinase-like enzyme from saccharomonospora viridis AHK190 in substrate-bound states elucidates the Ca2+-driven catalytic cycle. *Biochemistry.* 57:5289–5300.
37. Jog, J. P. 1995. Crystallization of polyethyleneterephthalate. *J. Macromol. Sci. Polym. Rev.* 35:531–553.
38. Wei, R., T. Oeser, …, W. Zimmermann. 2014. Functional characterization and structural modeling of synthetic polyester-degrading hydrolases from Thermomonospora curvata. *Amb. Express.* 4:44.
39. Wishart, D. S., C. G. Bigam, …, B. D. Sykes. 1995. 1H, 13C and 15N random coil NMR chemical shifts of the common amino acids. I. Investigations of nearest-neighbor effects. *J. Biomol. NMR.* 5:67–81.
40. Carbajo, R. J., F. A. Kellas, …, D. Neuhaus. 2005. Structure of the F1-binding domain of the stator of bovine F1Fo-ATPase and how it binds an α-subunit. *J. Mol. Biol.* 351:824–838.
41. Pople, J. A. 1956. Proton magnetic resonance of hydrocarbons. *J. Chem. Phys.* 24:1111.
42. Platzer, G., M. Mayer, …, R. Konrat. 2020. PI by NMR: probing CH–π interactions in protein–ligand complexes by NMR spectroscopy. *Angew. Chem.* 132:14971–14978.
43. Amero, C., M. Asunción Durá, …, J. Boisbouvier. 2011. A systematic mutagenesis-driven strategy for site-resolved NMR studies of supramolecular assemblies. *J. Biomol. NMR.* 50:229–236.

44. Pritišanac, I., M. T. Degiacomi, …, A. J. Baldwin. 2017. Automatic assignment of methyl-NMR spectra of supramolecular machines using graph theory. *J. Am. Chem. Soc.* 139:9523–9533.

45. Lescanne, M., S. P. Skinner, …, M. Ubbink. 2017. Methyl group assignment using pseudocontact shifts with PARAssign. *J. Biomol. NMR.* 69:183–195.

46. Monneau, Y. R., P. Rossi, …, C. G. Kalodimos. 2017. Automatic methyl assignment in large proteins by the MAGIC algorithm. *J. Biomol. NMR.* 69:215–227.

47. Flügge, F., and T. Peters. 2018. Complete assignment of Ala, Ile, Leu, Met and Val methyl groups of human blood group A and B glycosyltransferases using lanthanide-induced pseudocontact shifts and methyl-methyl NOESY. *J. Biomol. NMR.* 70:245–259.

48. Pritišanac, I., J. M. Würz, …, P. Güntert. 2019. Automatic structure-based NMR methyl resonance assignment in large proteins. *Nat. Commun.* 10:4922.

49. Pritišanac, I., T. R. Alderson, and P. Güntert. 2020. Automated assignment of methyl NMR spectra from large proteins. *Prog. Nucl. Magn. Reson. Spectrosc.* 118-119:54–73.

50. Nerli, S., V. S. De Paula, …, N. G. Sgourakis. 2021. Backbone-independent NMR resonance assignments of methyl probes in large proteins. *Nat. Commun.* 12:691.

51. Chen, C.-C., X. Han, …, R.-T. Guo. 2021. General features to enhance enzymatic activity of poly(ethylene terephthalate) hydrolysis. *Nat. Catal.* 4:425–430.

52. Kawai, F. 2021. The current state of research on PET hydrolyzing enzymes available for biorecycling. *Catalysts.* 11:206.

53. Joo, S., I. J. Cho, …, K.-J. Kim. 2018. Structural insight into molecular mechanism of poly(ethylene terephthalate) degradation. *Nat. Commun.* 9:382.

54. Chen, C.-C., X. Han, …, R.-T. Guo. 2018. Structural studies reveal the molecular mechanism of PETase. *FEBS J.* 285:3717–3723.

55. Dong, Q., S. Yuan, …, J. Zhou. 2020. Structure-guided engineering of a Thermobifida fusca cutinase for enhanced hydrolysis on natural polyester substrate. *Bioresour. Bioprocess.* 7:37.

56. Boehr, D. D., H. J. Dyson, and P. E. Wright. 2006. An NMR perspective on enzyme dynamics. *Chem. Rev.* 106:3055–3079.

57. Palmer, A. G. 2015. Enzyme dynamics from NMR spectroscopy. *Acc. Chem. Res.* 48:457–465.

58. Kitadokoro, K., U. Thumarat, …, F. Kawai. 2012. Crystal structure of cutinase Est119 from Thermobifida alba AHK119 that can degrade modified polyethylene terephthalate at 1.76Å resolution. *Polym. Degrad. Stabil.* 97:771–775.

59. Roth, C., R. Wei, …, N. Sträter. 2014. Structural and functional studies on a thermostable polyethylene terephthalate degrading hydrolase from Thermobifida fusca. *Appl. Microbiol. Biotechnol.* 98:7815–7823.

60. Oda, M., Y. Yamagami, …, F. Kawai. 2018. Enzymatic hydrolysis of PET: functional roles of three Ca2+ ions bound to a cutinase-like enzyme, Cut190*, and its engineering for improved activity. *Appl. Microbiol. Biotechnol.* 102:10067–10077.

61. Zeng, W., X. Li, …, R.-T. Guo. 2022. Substrate-binding mode of a thermophilic PET hydrolase and engineering the enzyme to enhance the hydrolytic efficacy. *ACS Catal.* 12:3033–3040.

62. Holliday, M. J., F. Zhang, …, E. Z. Eisenmesser. 2014. 1H, 13C, and 15N backbone and side chain resonance assignments of thermophilic Geobacillus kaustophilus cyclophilin-A. *Biomol. NMR Assign.* 8:23–27.

63. Holliday, M. J., C. Camilloni, …, E. Z. Eisenmesser. 2015. Structure and dynamics of GeoCyp: a thermophilic cyclophilin with a novel substrate binding mechanism that functions efficiently at low temperatures. *Biochemistry.* 54:3207–3217.

64. Berselli, A., M. J. Ramos, and M. C. Menziani. 2021. Novel. Pet-degrading enzymes: structure-function from a computational perspective. *Chembiochem.* 22:2032–2050.

65. Fecker, T., P. Galaz-Davison, …, C. A. Ramírez-Sarmiento. 2018. Active site flexibility as a hallmark for efficient PET degradation by I. Sakaiensis PETase. *Biophys. J.* 114:1302–1312.

66. Barth, M., T. Oeser, …, W. Zimmermann. 2015. Effect of hydrolysis products on the enzymatic degradation of polyethylene terephthalate nanoparticles by a polyester hydrolase from Thermobifida fusca. *Biochem. Eng. J.* 93:222–228.

67. Wei, R., T. Oeser, …, W. Zimmermann. 2016. Engineered bacterial polyester hydrolases efficiently degrade polyethylene terephthalate due to relieved product inhibition: engineered polyester hydrolases. *Biotechnol. Bioeng.* 113:1658–1665.

68. Saavedra, J. M., M. A. Azócar, …, L. P. Parra. 2018. Relevance of local flexibility near the active site for enzymatic catalysis: biochemical characterization and engineering of cellulase Cel5A from Bacillus agaradherans. *Biotechnol. J.* 13:1700669.

69. Araújo, R., C. Silva, …, A. Cavaco-Paulo. 2007. Tailoring cutinase activity towards polyethylene terephthalate and polyamide 6, 6 fibers. *J. Biotechnol.* 128:849–857.

70. Silva, C., S. Da, …, A. Cavaco-Paulo. 2011. Engineered Thermobifida fusca cutinase with increased activity on polyester substrates. *Biotechnol. J.* 6:1230–1239.

71. Zumstein, M. T., D. Rechsteiner, …, M. Sander. 2017. Enzymatic hydrolysis of polyester thin films at the nanoscale: effects of polyester structure and enzyme active-site accessibility. *Environ. Sci. Technol.* 51:7476–7485.

72. Falkenstein, P., R. Wei, …, C. Song. 2021. Mechanistic investigation of enzymatic degradation of polyethylene terephthalate by nuclear magnetic resonance. *Methods Enzymol.* 648:231–252.

Biophysical Journal, Volume *121*

Supplemental information

An NMR look at an engineered PET depolymerase

Cyril Charlier, Sabine Gavalda, Vinciane Borsenberger, Sophie Duquesne, Alain Marty, Vincent Tournier, and Guy Lippens

Supplementary Information for

An NMR look at an engineered PETase

Cyril Charlier, Sabine Gavalda, Vinciane Borsenberger, Sophie Duquesne, Alain Marty, Vincent Tournier & Guy Lippens

Corresponding author : Guy Lippens
Email: glippens@insa-toulouse.fr

This PDF file includes:

Tables S1 to S2

Figures S1 to S17

Residue Number	CSP (ppm)
Amide backbone (CSP > 0.1 ppm)	
192	0.188
193	0.358
196	0.160
198	0.222
211	0.113
225	0.281
226	0.285
238	0.182
239	0.498
240	0.322
241	0.138
242	0.105

Table S1 : Residues of LCC with a Ca^{2+} induced CSP > 0.1ppm

Residue Number	CSP (ppm)
Amide backbone (CSP > 0.04 ppm)	
94	0.089
97	0.053
165	0.197
167	0.064
169	0.043
188	0.041
191	0.044
194	0.061
206	0.054
207	0.078
210	0.148
212	0.422
213	0.462
217	0.043
218	0.056
237	0.057
238	0.086
241	0.051
243	0.365
244	0.080
283	0.098
285	0.051
Methyls (CSP > 0.1 ppm)	
166	0.174
212	0.296
Imidazole Histidine (CSP > 0.4 ppm)	
242	0.772

Table S2 CSP values for the different NMR probes in the titration experiment of LCC-ICC with MHET.

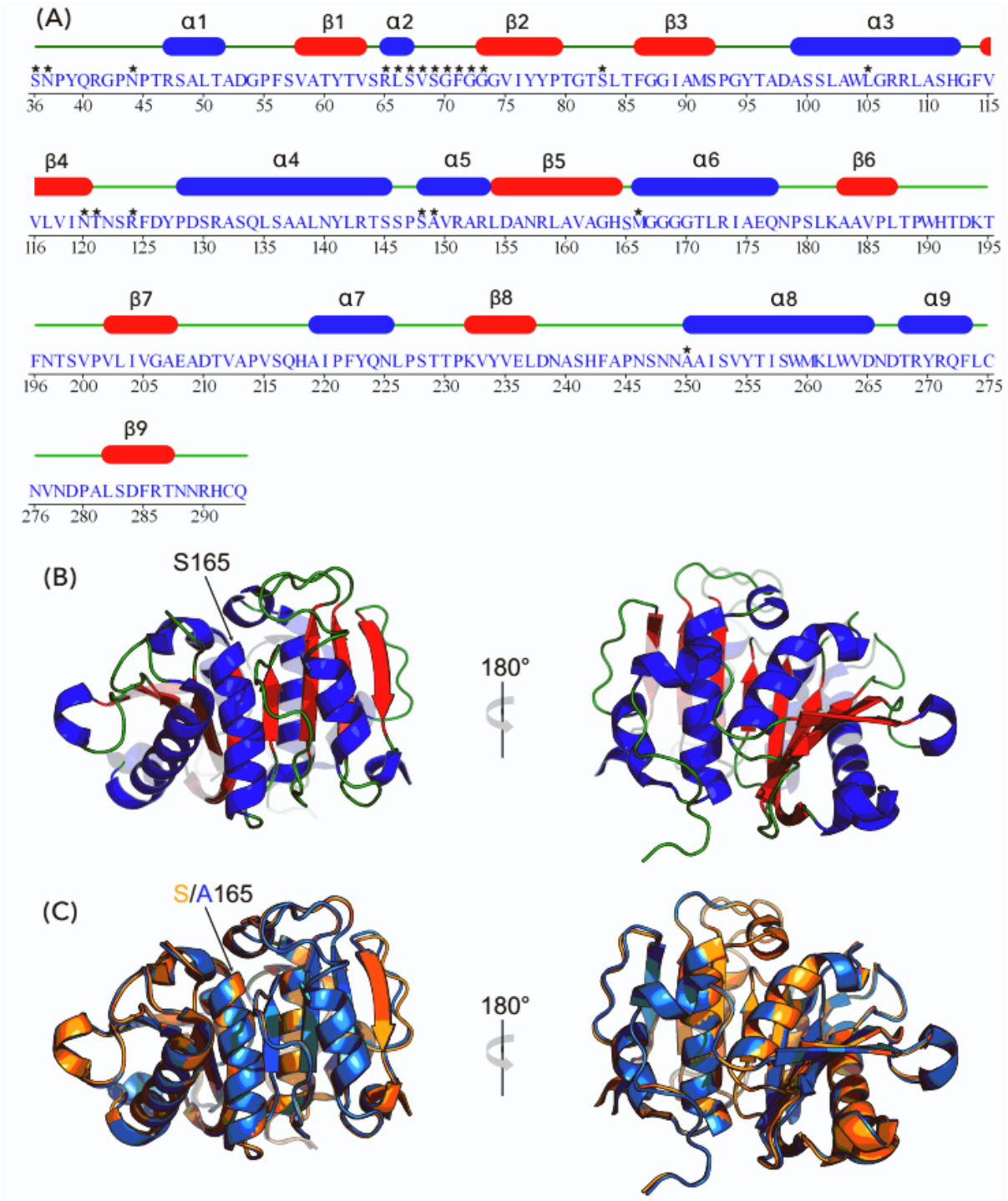

Figure S1. Structural analysis of the LCC enzyme. (A) Secondary structure elements as determined by Stride (http://webclu.bio.wzw.tum.de/stride/) with α helices in blue and β strands in red. Residues whose backbone assignment could not be obtained in this study are labeled with an * in the primary sequence. (B) 3D structure of LCC-WT (4EB0) with assigned secondary structure elements colored as in (A). (C) Overlay of LCC-WT (orange, 4EB0) and LCC-S165A (light blue, 6THS) 3D structures displaying a root mean square deviation (RMSD) over all atoms of 0.27Å. The position of the mutated residue (S165A) is indicated.

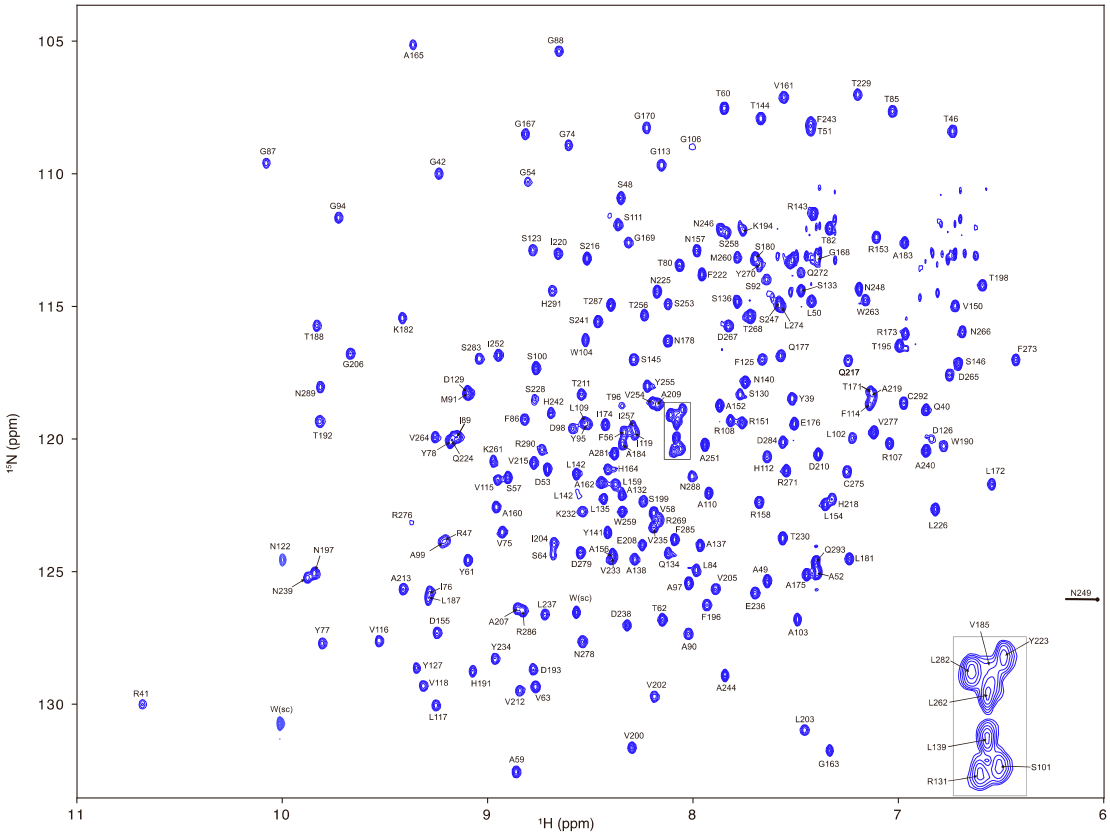

Figure S2. NMR assignment of the TROSY spectrum of LCC. 2D ^{1}H-^{15}N TROSY spectrum of LCC dissolved in 25 mM Tris-HCl buffer pH 7.5 supplemented with 100 mM NaCl. The amide proton of N249 resonates at 5.43ppm, and is outside the window shown. The resonance of A165 is folded in, and its true frequency is 135.1ppm in the nitrogen dimension. Residual signals of the Asn/Gln NH_2 groups at 6.5-7ppm/110-115ppm $^{1}H/^{15}N$ chemical shifts are not assigned.
Tryptophan side chain HN correlations are labeled as W (sc).

```
LCC         ----------------------------------------------S36NPYQRGPNPT46
Cut190      ----------------------------------------------D46NPYERGPDPT56
Tfcut2      ----------------------------------------------A1 NPYERGPNPT11

LCC         R47SALTA-DGPFSVATYTVSRLSVSGFGGGVIYYPTGTSL-TFGGIAMSPGYTADASSLAW104
Cut190      E57DSIEAIRGPFSVATERVSSF-ASGFGGGTIYYPRETDEGTFGAVAVAPGFTASQGSMSW115
Tfcut2      D12ALLEARSGPFSVSEENVSRLSASGFGGGTIYYPRENN—-TYGAVAISPGYTGTEASIAW69

LCC         L105GRRLASHGFVVLVINTNSRFDYPDSRASQLSAALNYLRTSSPSAVRARLDANRLAVAGH164
Cut190      Y116GERVASQGFIVFTIDTNTRLDQPGQRGRQLLAALDYLVERSDRKVRERLDPNRLAVMGH175
Tfcut2      L70GERIASHGFVVITIDTITTLDQPDSRAEQLNAALNHMINRASSTVRSRIDSSRLAVMGH129

LCC         S165MGGGGTLRIAEQNPSLKAAVPLTPWHTDKTF-NTSVPVLIVGAEADTVAPVSQHAIPFY223
Cut190      S176MGGGGSLEATVMRPSLKASIPLTPWNLDKTWGQVQVPTFIIGAELDTIAPVRTHAKPFY235
Tfcut2      S130MGGGGSLRLASQRPDLKAAIPLTPWHLNKNWSSVTVPTLIIGADLDTIAPVATHAKPFY189

LCC         Q224NLPSTTPKVYVELDNASHFAPNSNNAAISVYTISWMKLWVDNDTRYRQFLC-NVNDPAL282
Cut190      E236SLPSSLPKAYMELDGATHFAPNIPNTTIAKYVISWLKRFVDEDTRYSQFLCPNPTDRAI295
Tfcut2      N190SLPSSISKAYLELDGATHFAPNIPNKIIGKYSVAWLKRFVDNDTRYTQFLCPGPRDGLF249

LCC         -----S283DFR-TNNRHCQ293----------------------
Cut190      -----E296EYRSTCPYKLN305----------------------
Tfcut2      G250EVEEYRSTCPFYPNSSSVDKLAAALEHHHHHH287
```

Figure S3. Primary sequence alignment of different PETases. CLUSTAL multiple sequence alignment of the LCC sequence (Uniprot G9BY57 ; PDB ID : 4EB0) with those of Cut190 (Uniprot W0TJ64 ; PDB ID : 5ZNO) and Tfcut2 (Uniprot E5BBQ3 ; PDB ID: 4CG1). Numbering follows that of the PDB files. Residues composing the catalytic triad (Ser, Asp and His) are indicated in magenta. Calcium binding site 1 as defined in Cut190 is indicated in dark blue, Calcium binding sites 2 and 3 in light blue and green respectively. The latter two sites in LCC as confirmed by the NMR titration experiment are underlined. The A97-D98 dipeptide in LCC and its equivalent G62-T63 in Tfcut2 are shaded in grey.

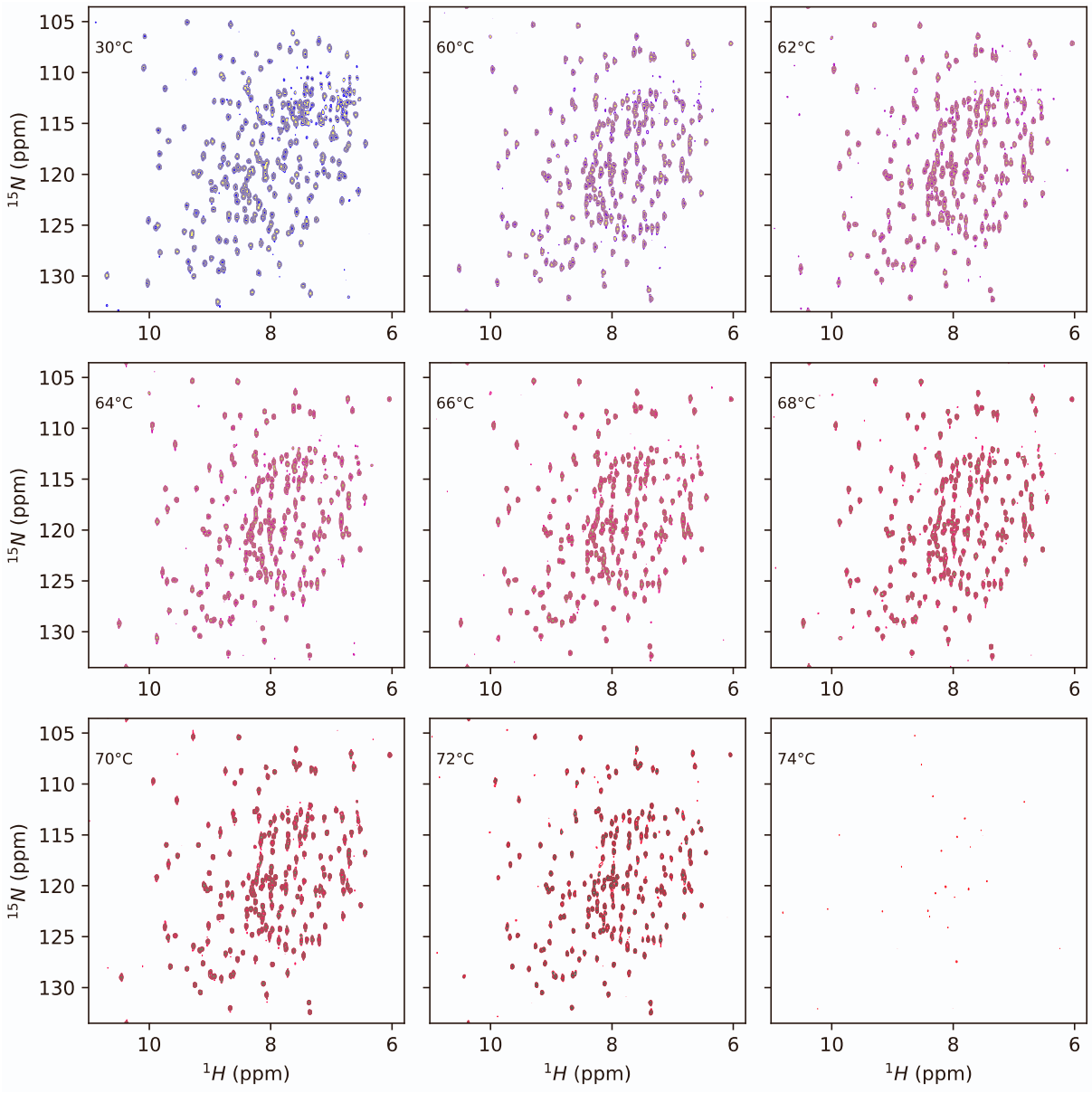

Figure S4. **^{1}H-^{15}N TROSY spectra of LCC as function of temperature from 30ºC up to 74ºC.**

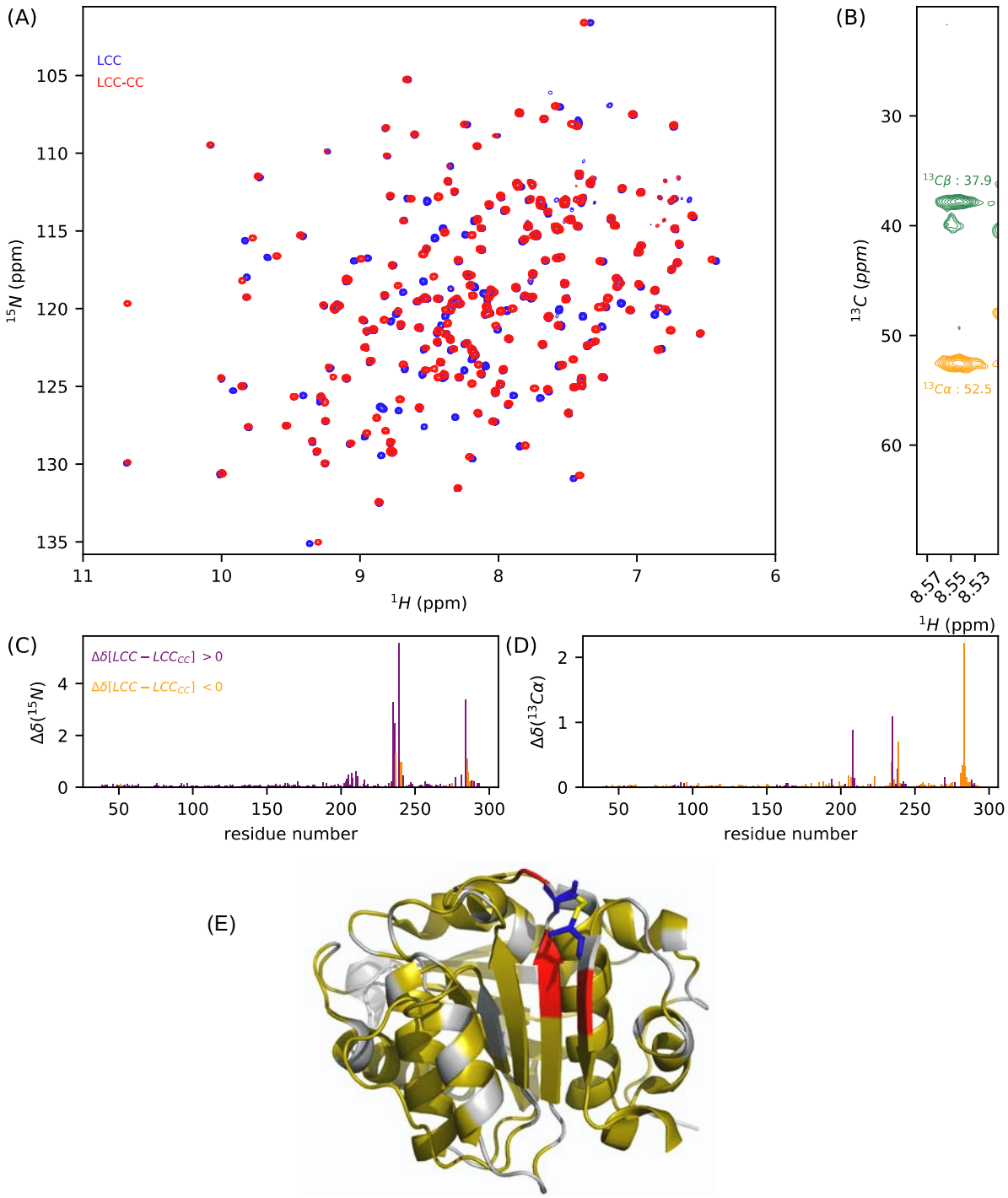

Figure S5. Introducing a C238-C283 disulfide bond in LCC does not change its overall structure. (A) Overlay of ^{1}H-^{15}N spectra of LCC (blue) and LCC-CC (red) recorded at 30ºC. (B) ^{1}H-^{13}C strip extracted for C238 from the HNCACB experiment of LCC-CC. Orange and green indicate positive and negative contours, respectively. Comparison of (C) ^{15}N and (D) ^{13}Cα chemical shift differences in ppm between LCC and LCC-CC. Purple and orange bars correspond to positive and negative values. (E) Mapping on the surface of LCC of the chemical shift changes (gray: no data available, yellow: 0 < Δδ (^{15}N) < 1, red: Δδ (^{15}N) > 1) induced by the D238C and S283C mutations (in blue) and ensuing disulfide bond formation (in yellow). The bond is modeled on the basis of the structure of LCC-ICCG (PDB ID: 6THT).

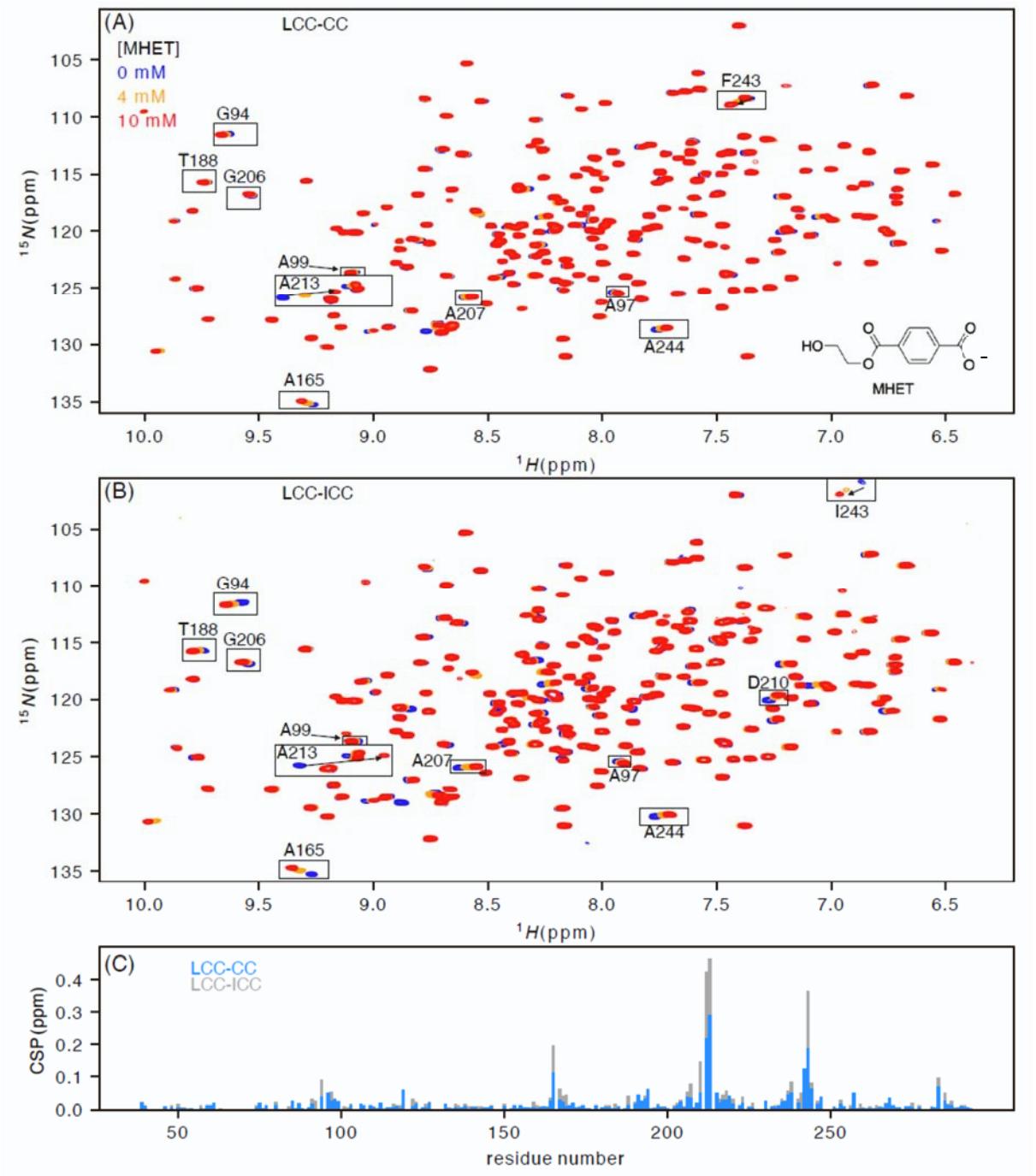

Figure S6. Mapping the molecular interactions of LCC variants with MHET. ^{1}H-^{15}N TROSY spectra of LCC-CC (A) and LCC-ICC (B) in absence (blue) and the presence of 4 mM (orange) and 10 mM (red) MHET measured at 60ºC. (C) ^{15}N/^{1}H chemical shifts perturbations induced by 10 mM of MHET in the spectrum of LCC-CC (blue) or LCC-ICC (grey).

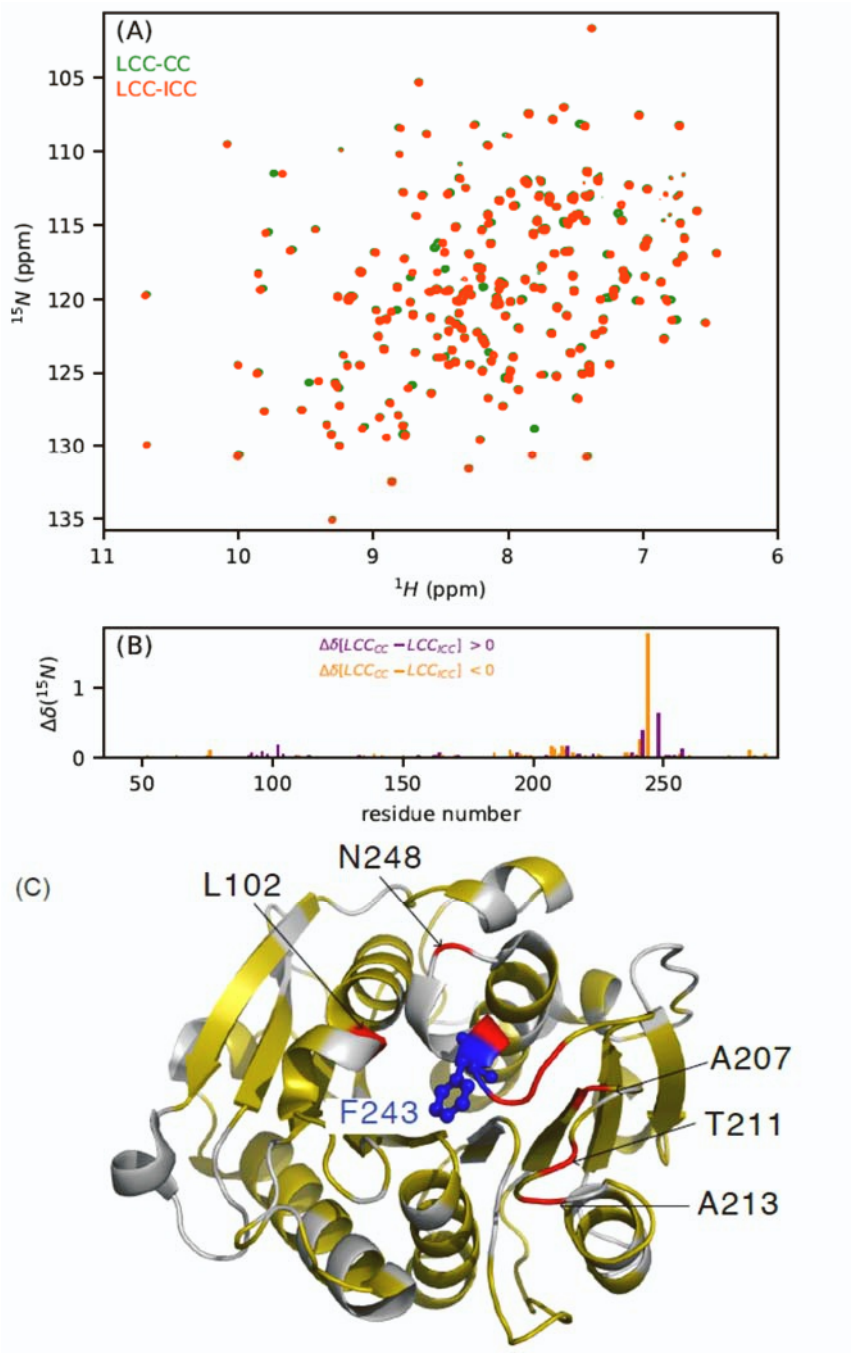

Figure S7. Impact of the F243I mutation limited to the shielding cone of the aromatic ring
(A) ^{1}H-^{15}N TROSY spectra of LCC-CC (green) and LCC-ICC (red) at 30ºC. (B) ^{15}N chemical shift differences (in ppm) between the LCC-CC and LCC-ICC. (C) ^{15}N chemical shift differences shown on the LCC structure (PDB ID: 6THS) with in gray the residues for which we have no data, in yellow residues with $0 < \Delta\delta < 0.15$ ppm and in red residue with $0.15 \text{ ppm} < \Delta\delta$. The residue F243 is shown in blue.

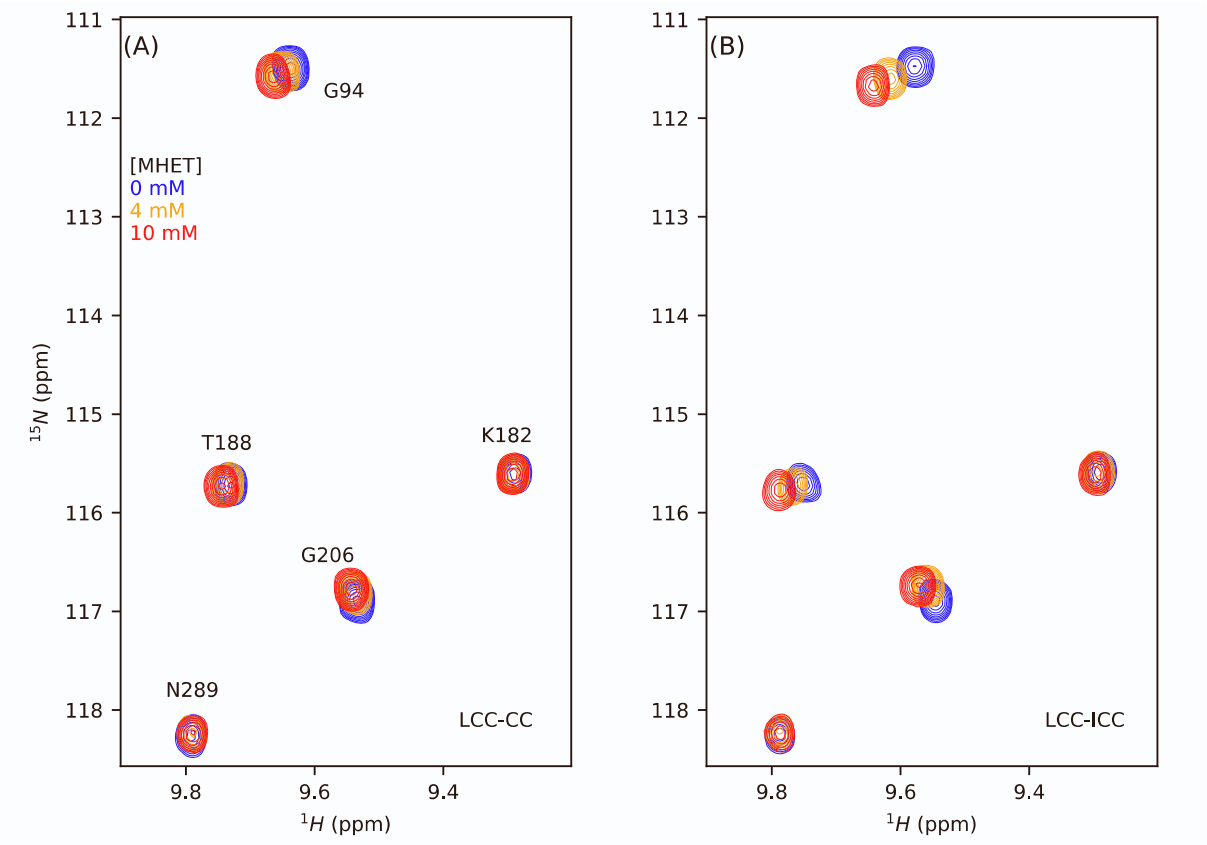

Figure S8. NMR mapping of MHET with the LCC mutants. Zoom of ^{1}H-^{15}N TROSY spectra of LCC-CC (A) and LCC-ICC (B) upon addition of MHET at 60ºC.

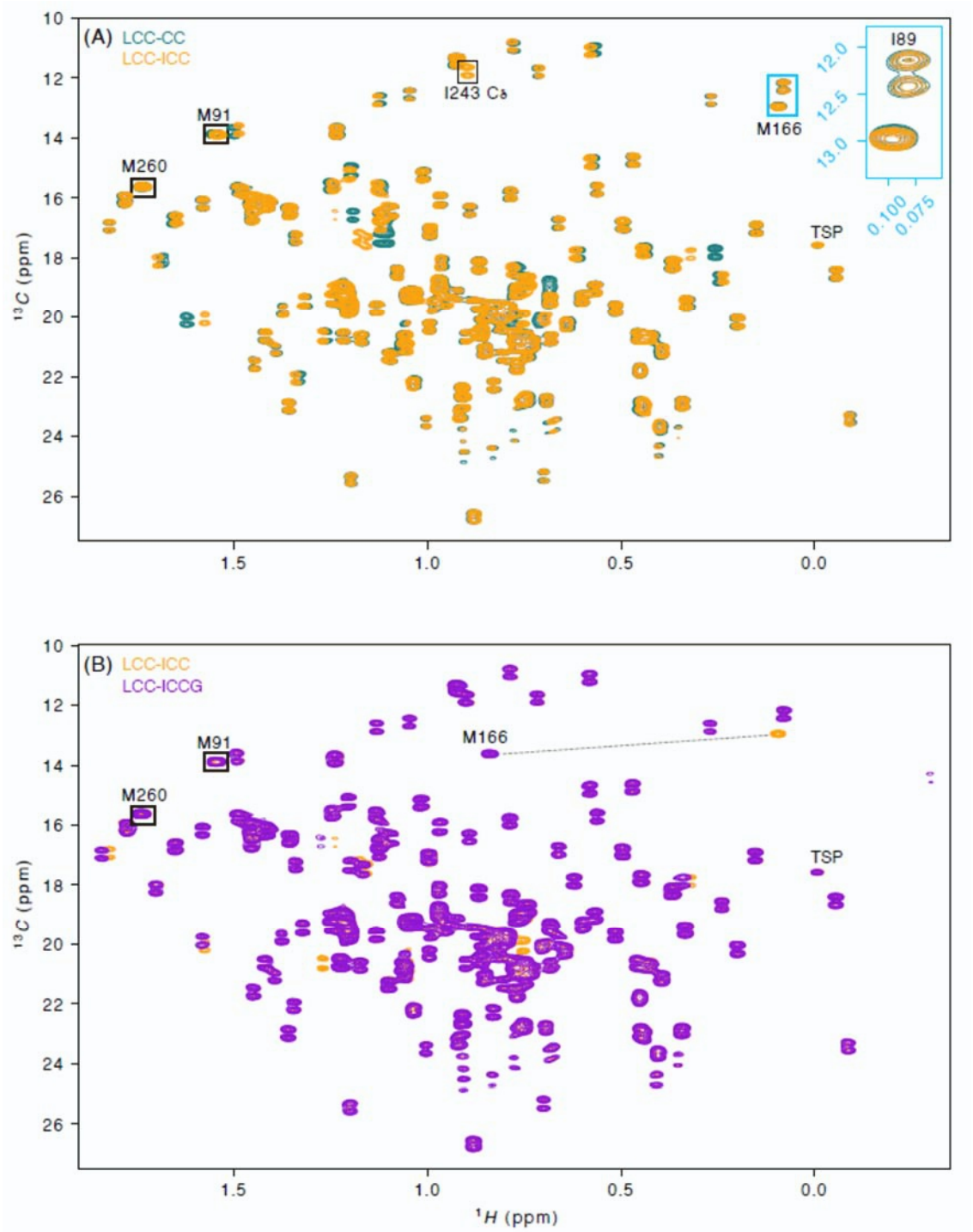

Figure S9. Methyl NMR spectra of the LCC mutants. Overlay of ^{1}H-^{13}C methyl HSQC spectra of (A) LCC-CC (teal) / LCC-ICC (orange) and (B) LCC-ICC (orange) and LCC-ICCG (purple) at 60ºC. The blue inset in (A) compares the methyl signal of M166 devoid of ^{13}C-^{13}C coupling with that of the I89 δ methyl whose carbon couples to its ^{13}Cγ nucleus.

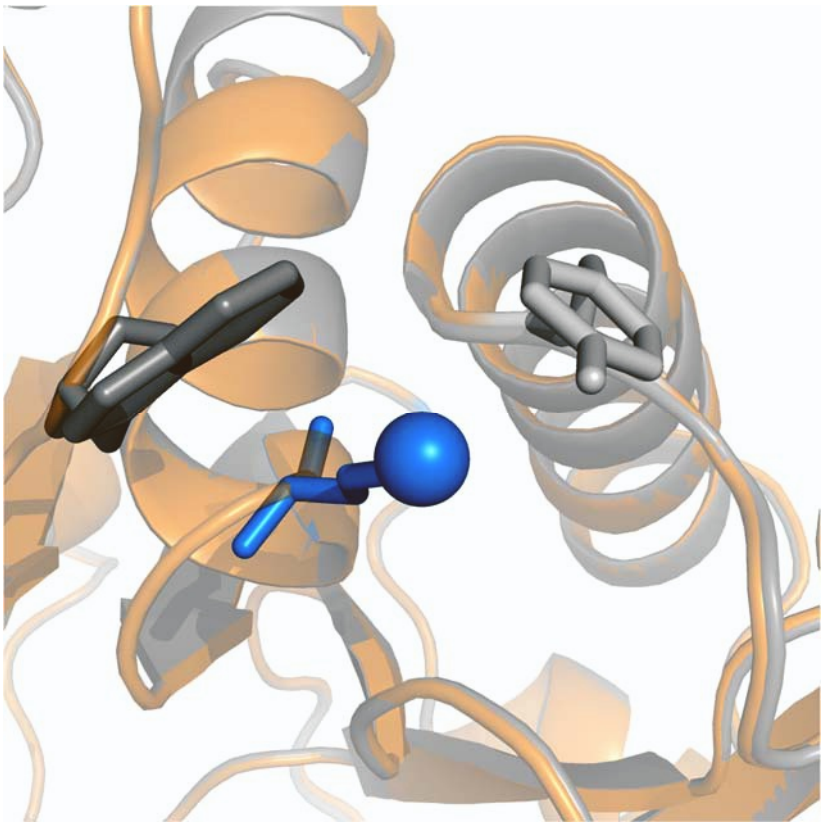

<u>Figure S10.</u> The methyl of M166 between the aromatic rings of W190 and Y127. Overlay of LCC (PDB ID: 6THS) in gray and LCC-ICCG (PDB ID: 6THT) in orange. M166 is shown in blue sticks and its methyl group as a sphere. W190 (black) and Y127 (gray sticks) from LCC are represented in sticks.

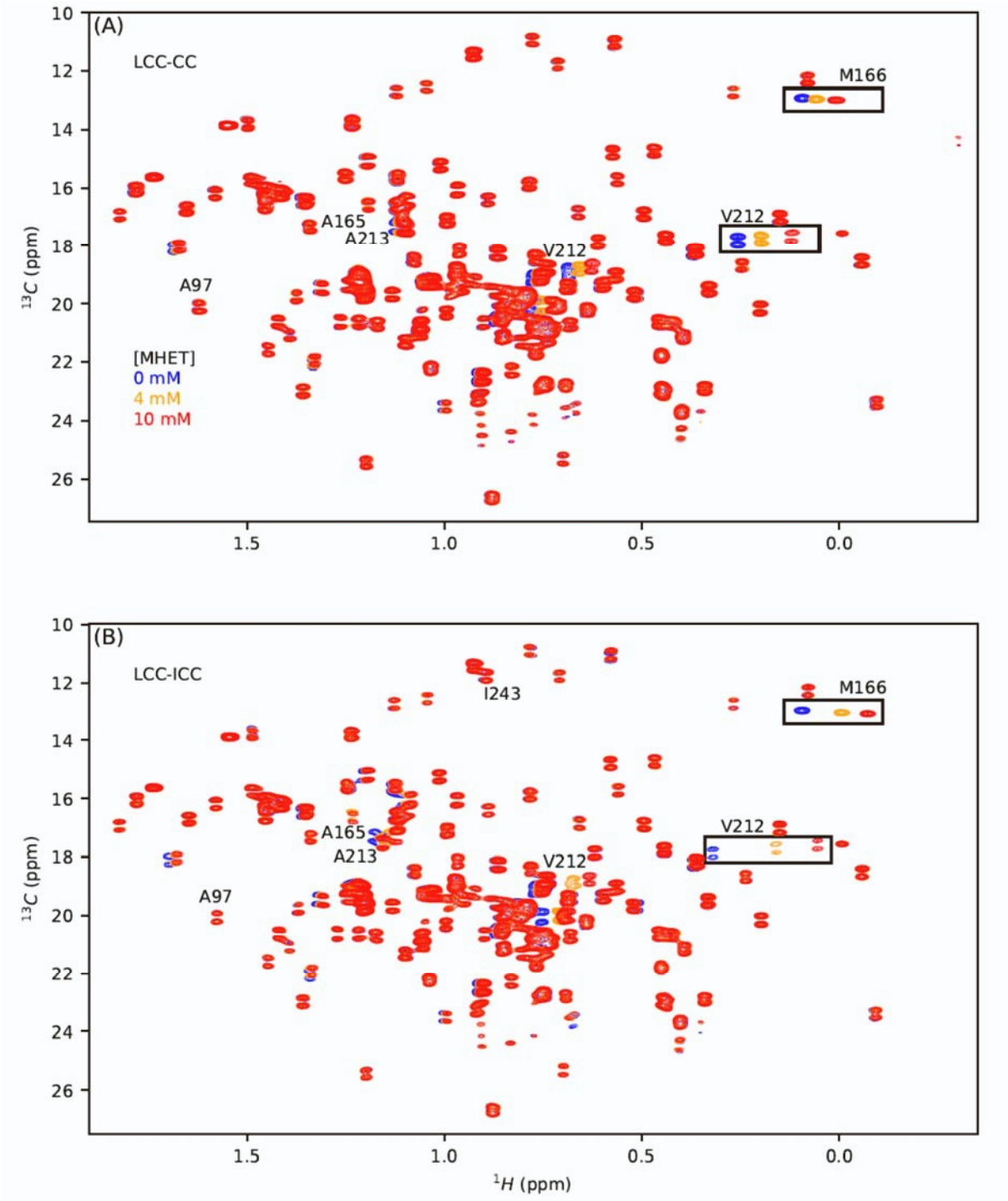

Figure S11. Methyl NMR mapping of MHET with the LCC mutants. ^{1}H-^{13}C HSQC spectra of LCC-CC (A) and LCC-ICC (B) in absence (blue) and the presence of 4 mM (orange) and 10 mM (red) MHET measured at 60ºC.

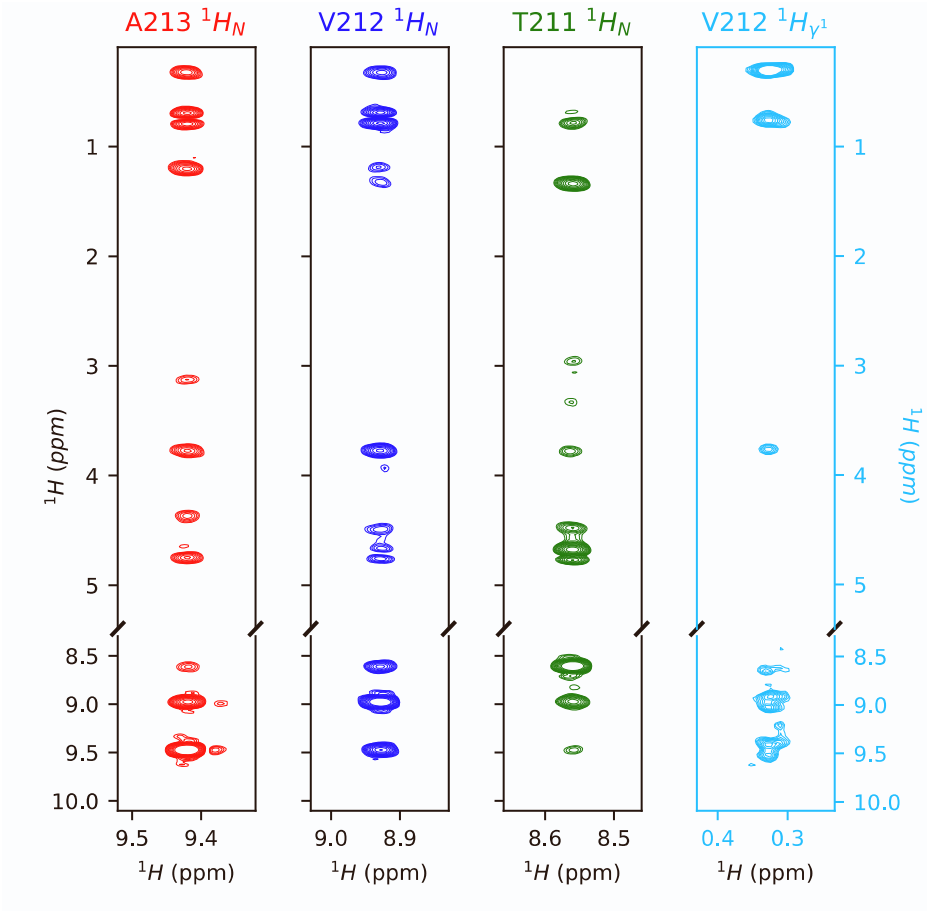

<u>Figure S12.</u> Strategy for assignment of V212 methyl groups of LCC-CC. ^{1}H-^{1}H strips from HNH-NOESY for residues T211/V212/A213. The lower parts show the correlations between amide protons, and the top parts with methyl protons. The ^{1}H-^{1}H corresponding strip for V212 in a HCH-NOESY is shown on the right side (light blue strip).

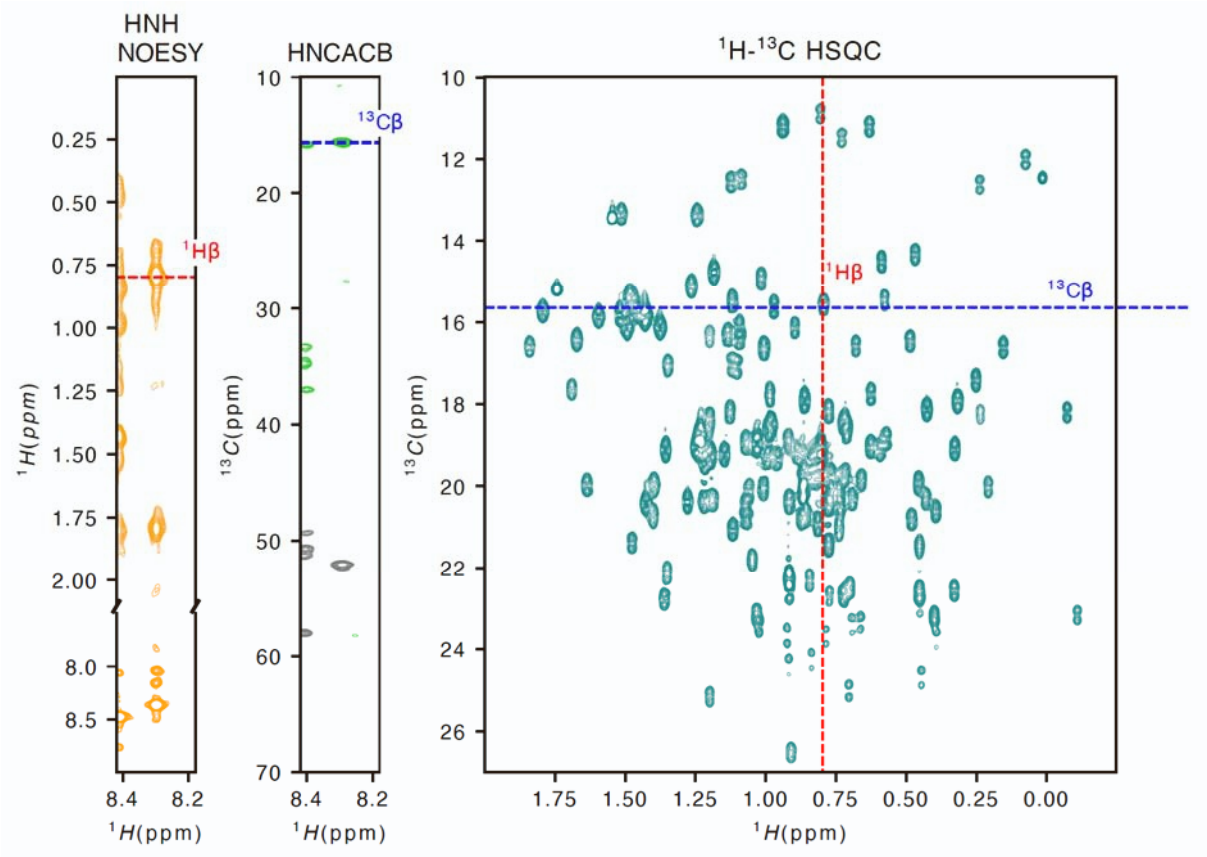

Figure S13. Strategy for assignment of Alanine methyl signals. The strip through the A138 amide correlation from the NOESY-^{1}H, ^{15}N TROSY experiment (left, orange) defines the methyl proton frequency, whereas the methyl carbon frequency can be read from the equivalent strip extracted from the HNCACB spectrum (grey for the Cα positive peak, light green for the Cβ negative peak). Both frequencies together define the position of the A138 methyl in the ^{1}H, ^{13}C HSQC spectrum (right, green).

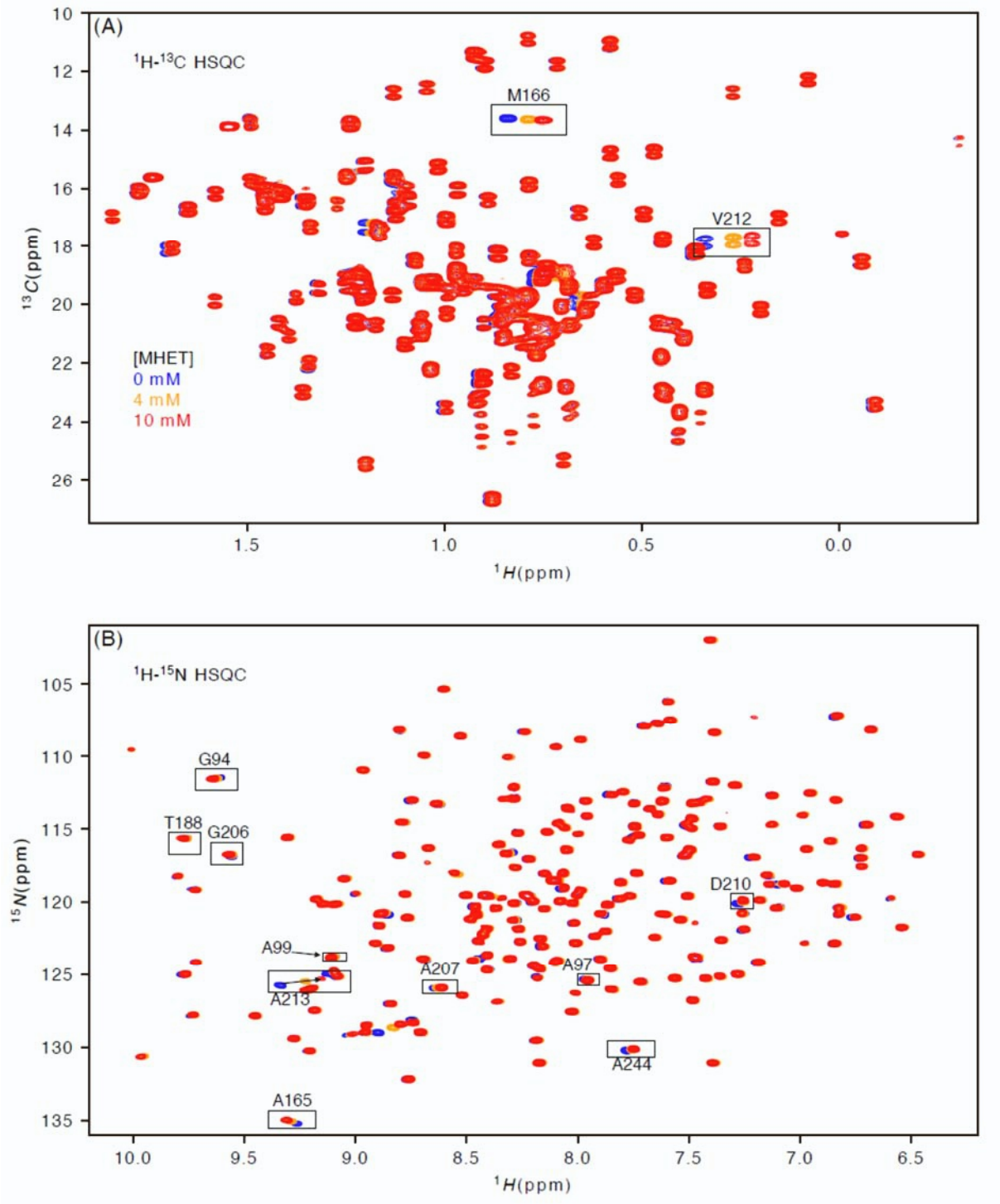

Figure S14. NMR mapping of MHET with LCC-ICCG. Interaction of LCC-ICCG with MHET reflected on ^{1}H-^{13}C HSQC spectra (A) and ^{1}H-^{15}N TROSY (B) Spectra are measured at 60ºC in absence (blue) and the presence of 4 mM (orange) and 10 mM (red) MHET.

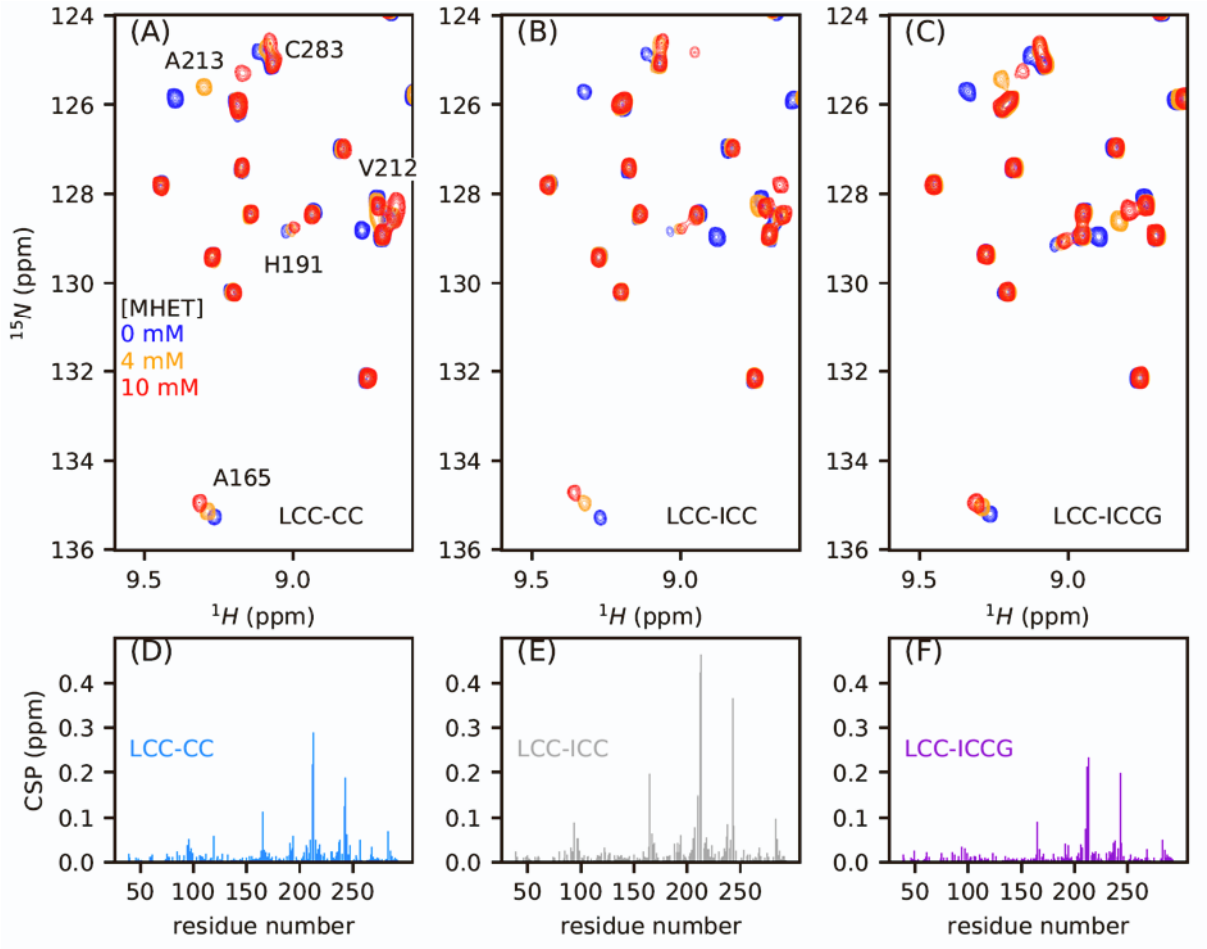

Figure S15. Summary of backbone NMR mapping of MHET with the LCC mutants. Interaction of MHET with LCC-CC (A, D), LCC-ICC (B, E) and LCC-ICCG (C, F). (A, B, C) Zoom on ^{1}H-^{15}N TROSY spectra in absence (blue) and the presence of 4 mM (orange) and 10 mM (red) of MHET measured at 60ºC. (D, E, F) ^{1}H-^{15}N combined chemical shift perturbations (CSPs) calculated from the spectrum in absence of MHET and in the presence of 10 mM.

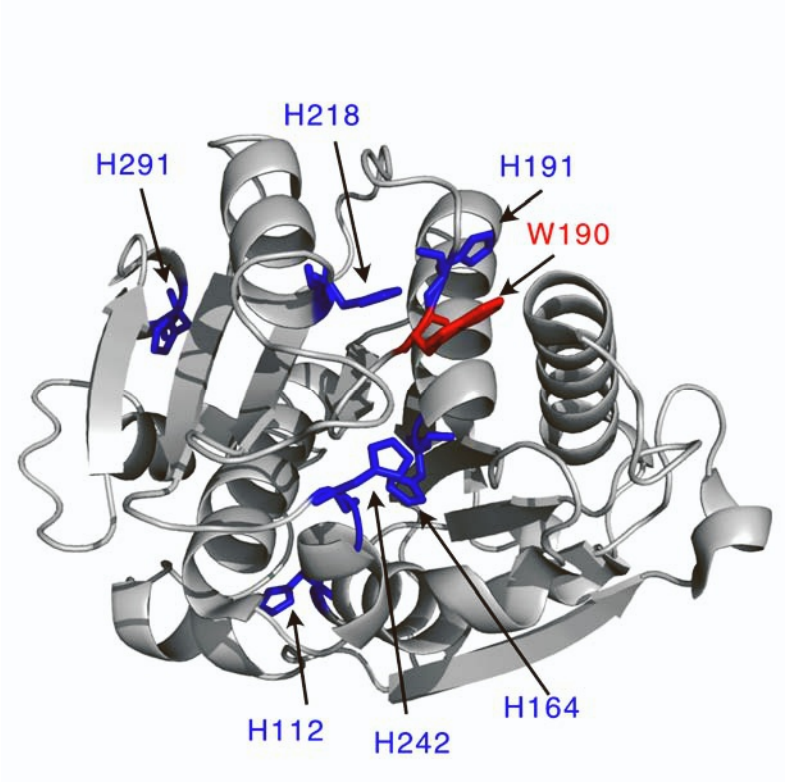

Figure S16. Histidines of LCC-ICCG. The 6 histidines of LCC-ICCG (PDB ID: 6THT) are colored in blue, W190 in red.

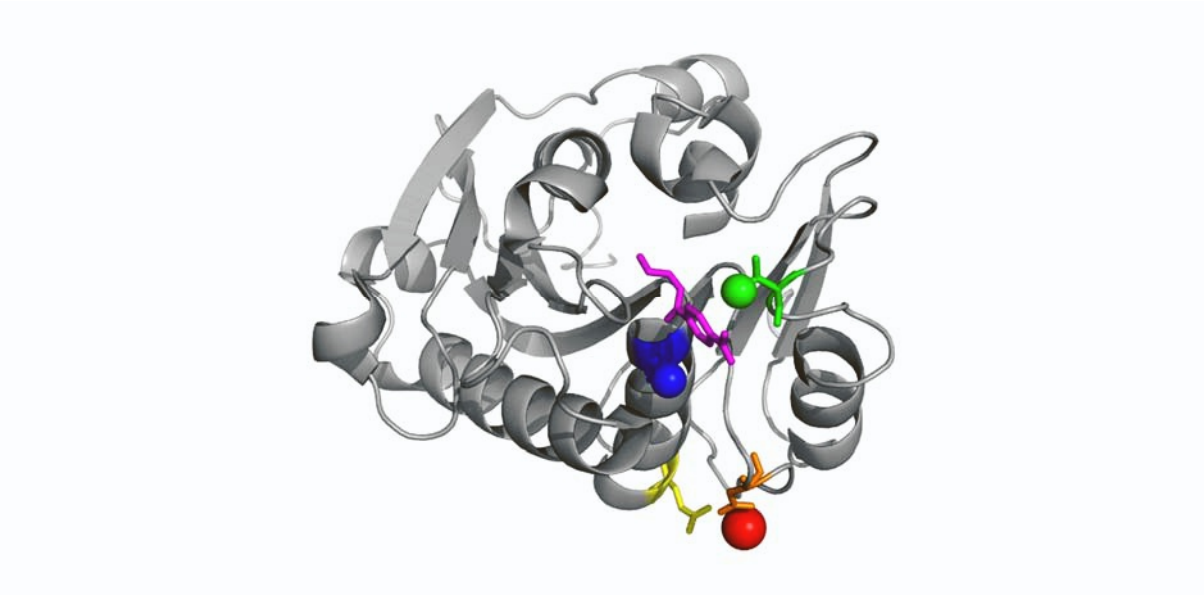

<u>Figure S17.</u> Crystal structure of LCC-ICCG in complex with MHET. The aromatic ring of the MHET moiety (in pink) is clamped between the methyls (presented as balls) of M166 (dark blue) and Val212 (green) in the recent crystal structure of the complex (PDB ID: 7VVE). A Ca^{2+} ion (red) complexed by the side chains of E176 (yellow) and D193 (orange) confirms the third binding site as defined in Cut190.